Baroclinic characteristics of frictionally destabilized abyssal overflows

By GORDON E. SWATERS

Applied Mathematics Institute, Department of Mathematical and Statistical Sciences, and Institute for Geophysical Research, University of Alberta, Edmonton, T6G 2G1, Canada
gordon.swaters@ualberta.ca

Observations show that the near-sill dynamics of dense abyssal overflows is variable and is governed, to a significant extent, by a balance between rotation, bottom friction and downslope acceleration due to gravity. Numerical simulations indicate that the near-sill downslope velocities are comparable to the phase/group velocities of long internal gravity waves. This suggests the possibility that overflows can become supercritical and destabilized by bottom friction. A theory is presented for the frictional destabilization of rotating abyssal overflows and the accompanying baroclinic coupling with the overlying ocean. This mode of transition allows for the formation of downslope and alongslope propagating periodic bores or pulses in the overflow and the generation of amplifying long internal gravity waves in the overlying ocean, and may help to explain aspects of the observed variability which seem unrelated to purely inertial baroclinic instability.

1. Introduction

The flow of relatively dense water over deep sills is a source point for the development of abyssal currents. These flows, such as, for example, the Denmark Strait Overflow (hereinafter DSO, e.g. Worthington 1969; Dickson & Brown 1994; Jungclaus, Hauser & Käse 2001), make an important global-scale contribution to the convective overturning of the oceans. Abyssal currents of this kind are responsible, as well, although on a smaller scale, for deep-water replacement in marginal seas (e.g. LeBlond *et al.* 1991; Masson 2002) and the along continental slope propagation of cold bottom-intensified mesoscale anomalies (Houghton *et al.* 1982; Swaters & Flierl 1991).

Greatly simplified, these flows initially exhibit pronounced downslope motion which subsequently evolves into more or less alongslope motion, which is banked against sloping topography. This picture is, of course, far from complete. Baroclinic interactions with the overlying water column and non-conservative processes such as entrainment and friction are present. In addition, there is considerable spatial and temporal variability associated with these flows in both the near-sill and downstream regions.

Bruce (1995), examining satellite imagery, and Krauss (1996), examining buoy trajectories, showed the development of downstream cyclonic eddies associated with the DSO. Although the source of this downstream variability has been the subject of some debate (e.g. Spall & Price 1998), recently analysed observations and numerical simulations (Krauss & Käse 1998; Käse & Oschlies 2000; Girton & Sanford 2001,

2002; Käse, Girton & Sanford 2002) suggest that key aspects of the variability can be understood in the context of the (non-quasi-geostrophic) baroclinic instability mechanism described by Swaters (1991) for abyssal currents, interpreted, of course, in the context of realistic physical oceanographic properties (e.g. Jiang & Garwood 1996; Jungclaus *et al.* 2001). In addition, this instability mechanism seems to be the process by which 'mesoscale' eddy formation occurs in laboratory experiments of unstable rotating abyssal currents (Choboter & Swaters 2000; Lane-Serff & Baines 1998; Etling *et al.* 2000).

In summary, the destabilization process described by Swaters (1991), which is subinertial, proceeds by the release of the available potential energy associated with the cross-slope position of a dense water anomaly sitting on a sloping bottom. In the overlying ocean, the instability manifests itself as amplifying topographic Rossby waves (see also Swaters 1998). It has been argued that wave–wave interactions and the red energy cascade, as well the local background topographic vorticity gradient, is conducive to preferential cyclogenesis in the overlying water column downstream of the DSO (Reszka, Swaters & Sutherland 2002).

Käse *et al.* (2002), analysing oceanographic data for the DSO region, from four different cruises over a three-year period, and examining high-resolution numerical simulations, describe the differing dynamical regimes between the near-sill and downstream overflow. In contrast to the downstream flow, the near-sill overflow is predominately downslope, strongly influenced by bottom friction and is near, and even possibly super, critical (with respect to long internal gravity waves). Girton & Sanford (2002), using estimates derived from the cruise data, argue, perhaps not surprisingly, that the near-sill momentum balance for the overflow is principally between rotation, downslope acceleration due to gravity and bottom friction.

These dynamical balances suggest another source for overflow variability, particularly in the near-sill region, and one which has not been explored before in this context. Frictional downslope flows which are supercritical can be unstable. In the absence of rotation and baroclinicity, the instabilities are classical roll waves (Jeffreys 1925; Whitham 1974). For oceanographically relevant scales, the instabilities will, as we show, manifest themselves in the overlying ocean as amplifying long internal gravity waves. Within the overflow itself, the instabilities take the form of downslope-propagating growing periodic bores or pulses.

The principal purpose of this paper is to develop a simple theory for the frictional destabilization of abyssal overflows, with rotation and baroclinicity present, and to determine the characteristics of the internal gravity field, in the overlying ocean, associated with the instability. In contrast to Swaters's subinertial baroclinic instability mechanism described above, the theory presented here will describe a dynamical connection between near-sill overflow variability to (slightly) superinertial long internal gravity waves. The generation and development of the internal gravity wave field associated with abyssal overflows remains poorly understood (Käse *et al.* 2002) but is important, not only in the interpretation of observations, but also in correctly parameterizing abyssal layer processes, particularly those involving gravity waves and bottom friction, in the present generation of ocean general circulation models.

It is important to emphasize that we are not suggesting that the frictionally induced destabilization described here is the principal dynamical mechanism for the observed cyclogenesis in abyssal overflows. We contend that the production of mesoscale vortices in abyssal overflows downstream from the near-sill region is the consequence of subinertial baroclinic instability. We do, however, suggest that frictionally induced

destabilization may have a role to play in the observed rapid entrainment of ambient overlying fluid during the initial stages of overflow development (as the instabilities grow in amplitude and ultimately break and become turbulent bores). It is interesting to further speculate that this entrainment process might lead to the development of an abyssal water mass that is large enough in scale for it to begin to interact with the surrounding water via subinertial baroclinic processes.

Although it is well known that gravity-driven frictionally balanced supercritical flow over a sloping bottom may be unstable (e.g. Jeffreys 1925; Whitham 1974; Baines 1995), several aspects of the process, particularly those which would be important in applying these ideas to the transition to instability of oceanographically relevant overflows, have not been explored. In particular, baroclinic coupling with the overlying water column within the context of a dissipative rotating fluid has not been examined.

More recent work on these flows has tended to focus on other aspects. For example, Needham & Merkin (1984) examined the role of horizontal friction within the one-layer shallow-water context. Kranenburg (1992) showed that the weakly nonlinear development of a marginally unstable flow could be described by a modified Burgers equation similar to that proposed by Novik (1971). Mandre (2001) extended these ideas to examine the nonlinear evolution when variable, or more specifically periodic, bottom topography is present.

The outline of the paper is as follows. Section 2 describes the model derivation. We assume a 'well-mixed' abyssal layer which is described by f-plane shallow-water equations on a sloping bottom with turbulent horizontal and quadratic bottom friction present. The overlying water column is described by the adiabatic incompressible Boussinesq equations for a continuously stratified rotating fluid.

We introduce a non-dimensional scheme based on classical gravity current theory for the abyssal layer and scale the overlying water column assuming the motion is principally driven by horizontal mass convergence/divergence created by variations in the abyssal current height. The resulting scaled equations have a number of non-dimensional parameters which are estimated based on available data. As a result, it is argued, that in the dynamical regime examined here, the abyssal layer is governed by fully nonlinear shallow-water theory, with friction and rotation present, and that the overlying ocean can be rationally described, to leading order, by the linear long-wave equations for a stratified rotating fluid forced by deformations in the interface between the two layers.

Section 3 details the formulation of the stability problem and describes the non-rotating instabilities. We begin by determining the general form of the uniform velocity and height solutions for the overflow and characterize their dependence on the (scaled) bottom friction coefficient and non-dimensional Coriolis parameter (or, equivalently, the reciprocal of the Rossby number). As expected, in the absence of bottom friction (rotation) there is no mean down (along) slope abyssal overflow. However, this dependence is not monotonic in the sense that sufficiently large rotation (due to geostrophy) or bottom friction (due to quadratic drag) results, ultimately, in decreasing overflow speeds.

The general linear instability problem is presented. The general linear instability problem depends on several non-dimensional parameters such as the (scaled) bottom friction coefficient, the Reynolds number, the (inverse) Rossby number, the Burgers number, and the along- and cross-slope wavenumbers, respectively. Without bottom friction, there is no instability and the perturbations in both the overflow current and surrounding ocean are 'neutral' internal gravity waves (with friction present within the overflow).
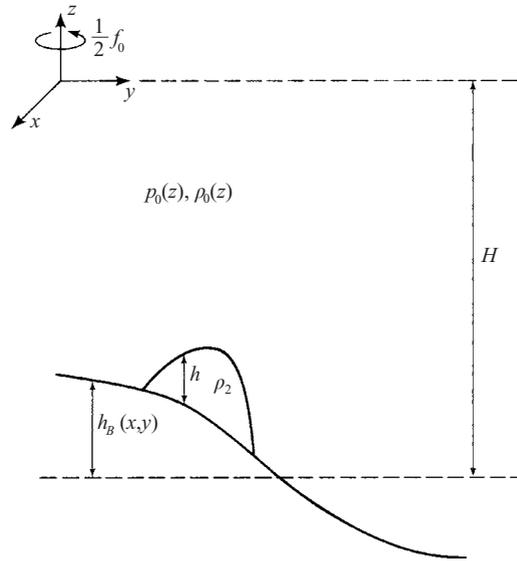
FIGURE 1. Geometry of the model used in this paper.

Because of the relatively large number of parameters in the general stability problem, it is useful to examine in some detail the baroclinic aspects of the stability problem in the non-rotating limit (but where friction is present). In this limit, the mean overflow current is oriented in the purely downslope direction and we can neglect, in the linear regime, the alongslope wavenumber and velocity in the perturbation field. As a result, the non-rotating instability problem for the overflow reduces to the classical roll wave stability equations which are coupled to long (non-rotating) internal gravity equations for the overlying ocean. We determine the stability characteristics for this configuration and describe the internal gravity waves so generated. We show that while the principle of exchange of stabilities holds in the non-rotating situation it does not hold when rotation is included in the dynamics. It is shown that the non-rotating stability characteristics form a singular, or discontinuous, limit of the rotating stability characteristics.

In §4, we turn to describing the general stability problem with rotation and bottom friction present. Our approach is to give a detailed description of the general stability characteristics which diverge from the non-rotating results as rotation, alongslope motion and variability (i.e. wavenumber) become increasingly important. For physically realistic values of the parameters, the instabilities are bottom intensified, have horizontal wavelengths of the order of 30 km, propagate prograde with respect to the overflow, have periods, in a geostationary frame of reference of about 2 h, and an *e*-folding growth time of about 1 day.

Our principal conclusions are summarized in §5.

2. Governing equations

The underlying geometry is sketched in figure 1. We assume f-plane dynamics for a stably and continuously stratified fluid of finite depth overlying a well-mixed abyssal current layer with variable bottom topography. The upper, i.e. the continuously stratified, layer is denoted as layer one. The abyssal current, i.e. the lower layer,

is denoted as layer two. The upper and abyssal layer dynamical quantities will be denoted, unless otherwise specified, with a 1 and 2 subscript, respectively.

The theoretical work starts with the incompressible adiabatic equations under a Boussinesq approximation for a continuously stratified fluid for the upper layer and the shallow-water equations for the abyssal layer. We assume a rigid ocean surface which will filter out the external gravity wave modes in the model and focus attention on the baroclinic aspects of the dynamics.

The dimensional equations of motion in the upper layer are given by (see, e.g. LeBlond & Mysak 1978)

$$(\partial_{t^*} + \boldsymbol{u}_1^* \cdot \nabla^* + w^* \partial_{z^*})\boldsymbol{u}_1^* + f^* \boldsymbol{e}_3 \times \boldsymbol{u}_1^* = -\frac{1}{\rho_2}\nabla^* p_1^*, \tag{2.1}$$

$$\rho_2(\partial_{t^*} + \boldsymbol{u}_1^* \cdot \nabla^* + w^* \partial_{z^*})w^* = -\partial_{z^*} p_1^* - g\rho^*, \tag{2.2}$$

$$\nabla^* \cdot \boldsymbol{u}_1^* + w_{z^*}^* = 0, \tag{2.3}$$

$$(\partial_{t^*} + \boldsymbol{u}_1^* \cdot \nabla^* + w^* \partial_{z^*})\rho^* = 0, \tag{2.4}$$

where $\boldsymbol{u}_1^* = (u_1^*, v_1^*)$, w^*, ρ_2, p_1^*, $\nabla^* = (\partial_{x^*}, \partial_{y^*})$ and ρ^* are, respectively, the upper layer horizontal velocity field, vertical velocity, constant reference Boussinesq density (which, for convenience, we take to be the density of the abyssal layer denoted as ρ_2), total pressure field, the horizontal gradient operator and the total variable density field in the upper layer. The notation is standard and alphabetical subscripts indicate partial differentiation unless otherwise indicated.

The abyssal current, i.e. the lower layer, is governed by shallow-water theory with bottom and horizontal friction present. The dimensional governing equations are given by (see, e.g. Needham & Merkin 1984; Spall & Price 1998)

$$(\partial_{t^*} + \boldsymbol{u}_2^* \cdot \nabla^*)\boldsymbol{u}_2^* + f^* \boldsymbol{e}_3 \times \boldsymbol{u}_2^* = -\frac{1}{\rho_2}\nabla^* p^* + A_H \frac{\nabla^* \cdot (h^* \nabla^* \boldsymbol{u}_2^*)}{h^*} - \frac{c_D^* |\boldsymbol{u}_2^*| \boldsymbol{u}_2^*}{h^*}, \tag{2.5}$$

$$h_{t^*}^* + \nabla^* \cdot (\boldsymbol{u}_2^* h^*) = 0, \tag{2.6}$$

where $\boldsymbol{u}_2^* = (u_2^*, v_2^*)$, p^* and h^* are, respectively, the abyssal layer horizontal velocity, the dynamic pressure and thickness relative to the height of the bottom topography, with $|\boldsymbol{u}_2^*| = \sqrt{\boldsymbol{u}_2^* \cdot \boldsymbol{u}_2^*}$. The horizontal eddy coefficient is given by A_H and the bottom drag coefficient is given by c_D^*. Implicit in these equations is the assumption that, while the upper layer is stably stratified but essentially inviscid, the abyssal layer may be thought of as well mixed but where bottom friction and turbulent horizontal mixing are present.

2.1. *Boundary conditions*

Assuming a rigid ocean surface, the dimensional kinematic vertical boundary conditions associated with the upper layer are given by

$$\left.\begin{array}{l} w^* = 0 \quad \text{on} \quad z^* = 0, \\ w^* = (\partial_{t^*} + \boldsymbol{u}_1^* \cdot \nabla^*)[h^* + h_B^*] \quad \text{on} \quad z^* = -H + h^* + h_B^*, \end{array}\right\} \tag{2.7}$$

respectively, where H and $h_B^* = h_B^*(x^*, y^*)$ are the reference depth of the upper layer and the height of the variable bottom topography relative to the reference depth $z^* = -H$, respectively. The slopes associated with the bottom topography are assumed to be small enough so as not to violate the hydrostatic approximation which is implicit in deriving the shallow-water equations (2.5) and (2.6).

It will be necessary eventually to Taylor expand the kinematic boundary condition (2.7b) about $z^* = -H$. Expanding, we obtain

$$w^* = (\partial_{t^*} + \boldsymbol{u}_1^* \cdot \boldsymbol{\nabla}^* - w_{z^*}^*)[h^* + h_B^*] + O\left\{\left(\frac{w^*}{H^2}, \frac{\boldsymbol{u}_1^*}{LH}\right)(h^* + h_B^*)^2\right\} \quad \text{on} \quad z^* = -H,$$

(2.8)

where L is the horizontal length scale and we have taken H to be the upper-layer vertical length scale.

Since there is no frictional stress between the abyssal current and upper layer (see (2.5), there is only bottom and horizontal friction in the abyssal current), the appropriate dynamic boundary condition across the two layers is that the total pressure be continuous across the interface.

If we denote the background hydrostatic density field in the upper layer as $\rho_0(z^*)$ and the total pressure field in the abyssal layer as $p_2^*(x^*, y^*, z^*, t^*)$, it is convenient to write p_1^* and p_2^* in the form, respectively,

$$p_1^*(x^*, y^*, z^*, t^*) = g \int_{z^*}^0 \rho_0(\xi)\,\mathrm{d}\xi + \varphi^*(x^*, y^*, z^*, t^*),$$

(2.9)

$$p_2^*(x^*, y^*, z^*, t^*) = g \int_{-H}^0 \rho_0(\xi)\,\mathrm{d}\xi - g\rho_2(z^* + H) + p^*(x^*, y^*, t^*),$$

(2.10)

where $\varphi^*(x^*, y^*, z^*, t^*)$ is the dimensional reduced pressure in the upper layer and $p^*(x^*, y^*, t^*)$ is the dynamic pressure in the abyssal layer appearing in (2.5).

Pressure continuity across the interface $z^* = -H + h^* + h_B^*$ is therefore satisfied provided

$$g \int_{-H+h^*+h_B^*}^0 \rho_0(\xi)\,\mathrm{d}\xi + \varphi^*(x^*, y^*, -H + h^* + h_B^*, t^*)$$

$$= g \int_{-H}^0 \rho_0(\xi)\,\mathrm{d}\xi - g\rho_2(h^* + h_B^*) + p^*(x^*, y^*, t^*). \quad (2.11)$$

It will become necessary to Taylor expand the first two terms in (2.11) about $z^* = -H$. To this end, we obtain

$$p^* = \varphi^* + g'\rho_2(h^* + h_B^*) + O\left\{\rho_2 N^2(-H)(h^* + h_B^*)^2, \varphi^*|_{z^*=-H}\left(\frac{h^* + h_B^*}{H}\right)\right\}$$

$$\text{on} \quad z^* = -H, \quad (2.12)$$

where the Brunt–Väisälä frequency, $N(z)$, and the reduced gravity, g', are given by

$$N^2(z) = -\frac{g}{\rho_2}\frac{\mathrm{d}\rho_0(z)}{\mathrm{d}z} > 0, \quad g' = \frac{g(\rho_2 - \rho_0(-H))}{\rho_2} > 0,$$

respectively. We will describe any horizontal boundary conditions as the need arises.

2.2. Scalings and non-dimensional equations

Roughly speaking, the two distinguished dynamical limits present in our model will correspond, in the first instance, to the case in which the dynamics of the abyssal current is frictionally dominated (that is, rotation plays a secondary role) and, in the second instance, to the case when rotation dominates the dynamics (that is, friction plays a secondary role), respectively.

Our approach to developing the non-dimensional equations is to introduce classical reduced-gravity or shallow-water scalings in the abyssal current which will allow us to examine both limits by adjusting non-dimensional parameters in the model appropriately. In the upper layer, we introduce a baroclinic scaling (see also Swaters 1991; Poulin & Swaters 1999; Karsten & Swaters 2000) so that the upper-layer motion is principally driven by horizontal mass convergence/divergence forced by variations in the abyssal current height.

To begin, if we scale the abyssal current height by h_* and let s^* be a typical value for the bottom slope, i.e.

$$s^* \simeq O(\nabla^* h_B^*),$$

we will choose the horizontal length scale to be given by $L = h_*/s^*$, and the abyssal current velocity scale to be given by $\sqrt{g'h_*}$, i.e. the speed of long internal gravity waves associated with the abyssal layer in the reduced gravity approximation. Time will be scaled advectively, i.e. $t^* \simeq O(T = \sqrt{h_*/g'}/s^*)$. The dynamic pressure field in the abyssal layer is scaled consistent with the pressure continuity relation (2.12).

The vertical velocity in the upper layer is scaled assuming that it is principally generated by stretching associated with a deforming interface, i.e.

$$w^* \simeq O(h_{t^*}^*),$$

which is consistent with (2.8). The horizontal velocity field in the upper layer is scaled consistent with the continuity equation (2.3), i.e.

$$\boldsymbol{u}_1^* \simeq O\left(\frac{L}{H}h_{t^*}^*\right).$$

The dynamic pressure field in the upper layer is scaled so that it balances the local accelerations and the dynamic density field in the upper layer is scaled so that it is in hydrostatic balance with the upper-layer dynamic pressure field.

The non-dimensional variables, which do not have an asterisk associated with them are, therefore, related to the dimensional variables through the relations

$$\boldsymbol{u}_2^* = \sqrt{g'h_*}\boldsymbol{u}_2, \quad p^* = \rho_2 g'h_* p, \quad h^* = h_* h, \tag{2.13}$$

$$h_B^* = s^* L h_B, \quad (x^*, y^*) = L(x, y), \quad z^* = Hz, \tag{2.14}$$

$$t^* = \left(\frac{\sqrt{h_*/g'}}{s^*}\right) t, \quad \boldsymbol{u}_1^* = \delta\sqrt{g'h_*}\boldsymbol{u}_1, \quad w^* = s^*\sqrt{g'h_*}w, \tag{2.15}$$

$$p_1^* = g\int_{z^*}^0 \rho_0(\xi)\,\mathrm{d}\xi + (\delta\rho_2 g'h_*)\varphi(x, y, z, t), \tag{2.16}$$

$$\rho^* = \rho_0(z^*) + \left(\frac{\delta^2\rho_2 g'}{g}\right)\rho(x, y, z, t), \tag{2.17}$$

where the parameter δ is the ratio of the layer scale thicknesses, given by

$$\delta \equiv h_*/H < 1. \tag{2.18}$$

Substitution of (2.13)–(2.18) into the dimensional equations leads to, for the upper layer,

$$(\partial_t + \delta\boldsymbol{u}_1\cdot\nabla + \delta w\partial_z)\boldsymbol{u}_1 + f\boldsymbol{e}_3\times\boldsymbol{u}_1 + \nabla\varphi = \boldsymbol{0}, \tag{2.19}$$

$$\left(\frac{H}{L}\right)^2 (\partial_t + \delta\boldsymbol{u}_1\cdot\nabla + \delta w\partial_z)w + \rho + \varphi_z = 0, \tag{2.20}$$

$$\nabla \cdot \boldsymbol{u}_1 + w_z = 0, \tag{2.21}$$

$$(\partial_t + \delta \boldsymbol{u}_1 \cdot \nabla) \rho + \delta w \rho_z = B(z) w, \tag{2.22}$$

and, for the abyssal layer,

$$(\partial_t + \boldsymbol{u}_2 \cdot \nabla)\boldsymbol{u}_2 + f \boldsymbol{e}_3 \times \boldsymbol{u}_2 = -\nabla p + \frac{1}{R_e} \frac{\nabla \cdot (h \nabla \boldsymbol{u}_2)}{h} - \frac{c_D |\boldsymbol{u}_2| \boldsymbol{u}_2}{h}, \tag{2.23}$$

$$h_t + \nabla \cdot (\boldsymbol{u}_2 h) = 0, \tag{2.24}$$

where the abyssal layer's Reynolds number, R_e, non-dimensional Coriolis parameter (or, equivalently, the reciprocal of the temporal Rossby number), f, scaled bottom drag coefficient (or, equivalently, the reciprocal of the non-rotating Froude number), c_D, and the Burgers number, $B(z)$, are given by, respectively,

$$\left. \begin{array}{l} R_e = \dfrac{h_* \sqrt{g' h_*}}{A_H s^*}, \quad c_D = \dfrac{c_D^*}{s^*}, \\[3mm] f = \dfrac{f^* \sqrt{h_*/g'}}{s^*}, \quad B(z) = \dfrac{s^* N^2 (Hz) H^2}{g' h_*}. \end{array} \right\} \tag{2.25}$$

The non-dimensional vertical boundary conditions for the upper layer are given by

$$w = 0 \quad \text{on} \quad z = 0, \tag{2.26}$$

$$w = h_t + \delta [\boldsymbol{u}_1 \cdot \nabla - w_z](h_B + h) + O(\delta^2) \quad \text{on} \quad z = -1, \tag{2.27}$$

and pressure continuity across the layer interface is given by

$$p = h + h_B + \delta \varphi + O(\delta^2) \quad \text{on} \quad z = -1. \tag{2.28}$$

There are a number of non-dimensional parameters and it is useful to attempt to estimate them for the abyssal overflows we are interested in. Although there is considerable variability and uncertainty, oceanographically relevant estimates for the order of magnitudes for the parameters are about (see, e.g. Whitehead *et al.* 1990; Karsten, Swaters & Thomson 1995; Jiang & Garwood 1996; Lane-Serff & Baines 1998; Spall & Price 1998; Etling *et al.* 2000; Jungclaus *et al.* 2001; Reszka *et al.* 2002; Käse *et al.* 2002)

$$\left. \begin{array}{l} c_D^* \approx 0.005, \quad s^* \approx 0.02, \\ g' \approx 0.004\,\text{m s}^{-2}, \quad h_* \approx 100\,\text{m}, \quad N \approx 10^{-3}\,\text{s}^{-1}, \\ H \approx 2000\,\text{m}, \quad f^* \approx 10^{-4}\,\text{s}^{-1}, \quad A_H \approx 25\,\text{m}^2\,\text{s}^{-1}. \end{array} \right\} \tag{2.29}$$

In turn, these would imply

$$\left. \begin{array}{l} \sqrt{g' h_*} \approx 60\,\text{cm s}^{-1}, \quad L \approx 5\,\text{km}, \quad T \approx 2.2\,\text{h}, \\ f \approx 0.8, \quad c_D \approx 0.25, \quad \delta \approx 0.05, \quad B \approx 2, \\ R_e \approx 400, \quad (H/L)^2 \approx 10^{-3}. \end{array} \right\} \tag{2.30}$$

These estimates suggest that the upper layer is hydrostatic to a good degree of approximation and that δ is smaller than either f or c_D and thus, to first approximation, we neglect the $O(\delta)$ terms. We shall develop the theory with horizontal friction present.

In this limit, the resulting upper-layer equations are simply the linear long-wave equations for a continuously stratified rotating fluid with a Boussinesq approximation (see, e.g. LeBlond & Mysak 1978 §15; see also, Rhines 1970) which are forced by variations in the height of the abyssal current (see (2.27)). To leading order, the

dynamic pressure field in the abyssal current decouples from the upper-layer dynamic pressure field (see (2.28)).

To leading order with respect to δ and under the hydrostatic approximation, (2.19)–(2.24), (2.26), (2.27) and (2.28) reduce to

$$(\partial_{tt} + f^2)(B^{-1}\varphi_{zt})_z + \Delta\varphi_t = 0, \qquad (2.31)$$

subject to

$$\varphi_{zt} = 0 \quad \text{on} \quad z = 0, \qquad (2.32)$$

$$\varphi_{zt} = -B(-1)h_t \quad \text{on} \quad z = -1, \qquad (2.33)$$

with the auxiliary upper-layer relations

$$(\partial_{tt} + f^2)\boldsymbol{u}_1 = f\boldsymbol{e}_3 \times \nabla\varphi - \nabla\varphi_t, \qquad (2.34)$$

$$\rho = -\varphi_z, \quad w = -B^{-1}\varphi_{zt}, \qquad (2.35)$$

where $h(x, y, t)$ is determined from the abyssal-layer equations

$$(\partial_t + \boldsymbol{u}_2 \cdot \nabla)\boldsymbol{u}_2 + f\boldsymbol{e}_3 \times \boldsymbol{u}_2 = -\nabla(h + h_B) + \frac{1}{R_e}\frac{\nabla \cdot (h\nabla\boldsymbol{u}_2)}{h} - \frac{c_D |\boldsymbol{u}_2| \boldsymbol{u}_2}{h}, \qquad (2.36)$$

$$h_t + \nabla \cdot (\boldsymbol{u}_2 h) = 0. \qquad (2.37)$$

These equations remain valid in both the non-rotating $f = 0$ and inviscid $c_D = A_H = 0$ ($R_e \to \infty$) limits.

3. Stability problem
3.1. *Description of the steady solutions*

The equations for general steady solutions to (2.36) and (2.37), appear to be analytically intractable. In the non-rotating and infinite R_e limit, it is possible to find spatially varying steady solutions to (2.36) and (2.37), but these appear to be of no interest on physical grounds.

The steady solutions which perhaps have genuine relevance (Girton & Sanford 2002), and upon which the theory of non-rotating roll waves has been developed, are the uniform height and velocity, i.e. 'slab,' solutions (see, e.g. Jeffreys 1925; Whitham 1974; Baines 1995) given by

$$\boldsymbol{u}_2 = \boldsymbol{U} = (U, V), \quad h = 1, \qquad (3.1)$$

for the linearly sloping bottom

$$h_B = -y, \qquad (3.2)$$

where we recall that the bottom topography and abyssal current thickness have been scaled explicitly using the slope and dimensional thickness, respectively. These uniform flows are equivalent to the solutions found for 'stream tube' models, without along-stream variation, which have been used to examine aspects of the dynamics of rotating turbidity and abyssal currents (e.g. Smith 1975; Killworth 1977; Price & Baringer 1994; Emms 1998).

Perhaps the most unappealing feature of these solutions is that the thickness field, i.e. h, does not possess groundings. That is, the mean height field does not vanish outside some region, the boundary of which is an incropping (see figure 1). One of the most satisfying features of the non-quasi-geostrophic baroclinic instability model developed by Swaters (1991) was that it was possible to determine explicitly the

stability characteristics for an abyssal flow with genuine groundings. Unfortunately, that appears not to be possible here.

The question must be raised concerning the applicability of the calculation presented here. Our view is that, considered as a theoretical process study, the stability characteristics described here will be of genuine relevance in understanding the range of dynamics possible in the transition to instability for abyssal overflows, even if it is not possible to apply these results immediately to a specific situation, in much the same way as in, for example, how the uniform flow solutions to the Phillips' model can be used to describe various properties of baroclinic instability on a β-plane (see, e.g. Pedlosky 1987 §7.11).

Substitution of (3.1) and (3.2) into (2.36) yields (continuity is trivially satisfied)

$$fV = c_D(U^2 + V^2)^{1/2}U, \tag{3.3}$$

$$fU = 1 - c_D(U^2 + V^2)^{1/2}V. \tag{3.4}$$

The friction-induced downslope motion and the rotation-induced rightward motion (in the northern hemisphere) of the mean flow is easily seen from the energy equation $-U \times (3.3) + V \times (3.4)$, i.e.

$$V = c_D(U^2 + V^2)^{3/2} > 0, \tag{3.5}$$

and from combining (3.5) with (3.3), yielding

$$U = f(U^2 + V^2) > 0. \tag{3.6}$$

The velocity can be found explicitly by substituting (3.5) and (3.6) into (3.4), or equivalently forming $(3.5)^2 + (3.6)^2$, giving

$$c_D^2(U^2 + V^2)^2 + f^2(U^2 + V^2) - 1 = 0,$$

from which it follows that

$$U^2 + V^2 \equiv \gamma^2 = \frac{2}{f^2 + \sqrt{f^4 + 4c_D^2}},$$

so that

$$U = f\gamma^2 = \frac{2f}{f^2 + \sqrt{f^4 + 4c_D^2}}, \tag{3.7}$$

$$V = c_D\gamma^3 = c_D\left(\frac{2}{f^2 + \sqrt{f^4 + 4c_D^2}}\right)^{3/2}. \tag{3.8}$$

The first thing to note is that in the absence of rotation and bottom friction (i.e. $f = c_D = 0$), (3.7) and (3.8) are singular, reflecting the fact that, without either rotation or bottom friction being present, there is, of course, no steady solution to the model. That is, there is no 'force' to counterbalance the downslope acceleration due to gravity, so that no steady flow can form.

Another thing to note about the solutions (3.7) and (3.8) is that although rotation is necessary for a non-zero alongslope velocity component, and bottom friction is necessary for a non-zero downslope velocity component, neither U nor V depend monotonically on f or c_D, respectively, and that U and V are individually maximized
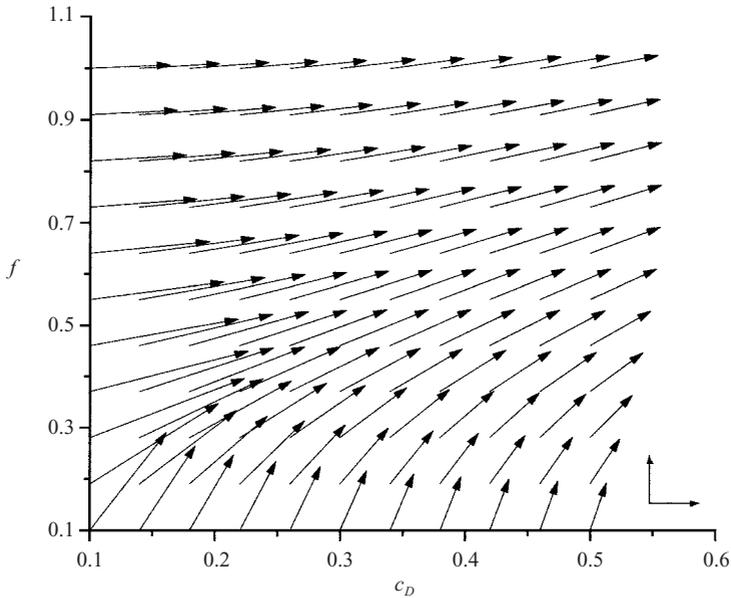
FIGURE 2. (U, V) in the (c_D, f)-plane.

for a finite non-zero value of f or c_D, respectively. Neither component of the velocity increases indefinitely as the physical process responsible for it becomes comparatively more important. The maximum alongslope velocity, regarded as a function of f, denoted as U_{max}, occurs when $f^2 = 2c_D/\sqrt{3}$, and is given by $U_{max} = 2/(3f)$. The maximum downslope velocity, regarded as a function of c_D, denoted as V_{max}, occurs when $c_D = \sqrt{2}f^2$, and is given by $V_{max} = 1/(2|f|)$. The non-monotonic dependence of the overflow velocity on bottom friction and rotation is not just a mathematical curiosity. As we show later in this section, it is key to developing a physical understanding of the differing dependences of the growth rate of the most unstable mode on the bottom friction coefficient between the non-rotating and rotating situations.

Figure 2 is a vector plot of the steady uniform velocity (U, V), determined by (3.7) and (3.8), as a function of the bottom friction coefficient c_D and the non-dimensional Coriolis parameter f for the range $0.1 \leqslant c_D \leqslant 0.5$ and $0.1 \leqslant f \leqslant 1.0$. In order to ensure that the vectors remain within the plot boundaries, the velocity vectors have been scaled so that the maximum speed, which occurs for the velocity vector located at $c_D = f = 0.1$ in figure 2 (the velocity vector located at the lower left-hand corner), has length 0.2. In addition, the vectors are oriented so that downslope motion is indicated by the vector pointing in the direction of increasing f. Rightward deflected (which occurs for positive f) alongslope motion is indicated by the vector pointing in the direction of increasing c_D. The orientation is shown in the lower right-hand corner in figure 2 by (U, V) coordinate axes.

Notwithstanding the remarks made above concerning the non-monotonic behaviour of the individual velocity components, we see the general trend from down (along) slope motion to along (down) slope motion as f (c_D) increases for a given c_D (f), within the context that the speed monotonically decreases as c_D and f individually increase.

3.1.1. *Inviscid and non-rotating steady flows*

The two sublimits of relevance correspond, respectively, to the rotation dominated situation, i.e. $c_D \longrightarrow 0$, and the friction dominated situation, i.e. $f \longrightarrow 0$. In the first case, the dimensional steady velocity is in the alongslope direction and is given by

$$V^* = 0, \quad U^* = \frac{g's^*}{f^*}, \tag{3.9}$$

which is just the Nof (1981) solution for density-driven flow on a linearly sloping bottom on an f-plane. This is the dynamical limit in which the Swaters (1991) (non-quasi-geostrophic) baroclinic instability theory (see also Swaters 1998; Poulin & Swaters 1999; Reszka *et al.* 2002) describes the destabilization of alongslope flowing abyssal currents, including the possible presence of groundings in the abyssal-layer height h (as shown in figure 1).

In the friction dominated situation, the dimensional steady velocity is in the downslope direction and is given by

$$U^* = 0, \quad V^* = \sqrt{g'h_*s^*/c_D^*}, \tag{3.10}$$

which is just the steady velocity found in classical roll wave theory (Jeffreys 1925) for a linearly sloping bottom in a non-rotating frame of reference. As mentioned previously, when the downslope velocity in (3.10) is sufficiently supercritical, the flow is unstable and the instabilities develop into periodic breaking waves or bores on the surface of the uniform current (Whitham 1974; Baines 1995; see, also, Mandre 2001). Our goal here is to examine the linear stability properties of (3.7) and (3.8) with rotation and horizontal dissipation present and determine the baroclinic structure of the instabilities in the overlying ocean.

Finally, we note that any time-independent flow is a steady solution to the upper-layer equations (2.31), (2.32) and (2.33). However, since the upper-layer equations are linear, they are not able to describe any baroclinic or barotropic instability in the overlying ocean. In addition, the forthcoming frictional stability characteristics are not altered by the presence of a mean flow in the upper layer. Accordingly, for convenience, and to focus attention on the upper-layer structure of frictionally destabilized overflows, we assume no mean steady flow in the upper layer.

3.2. *The general linear stability equations*

Substituting

$$(u, v, h) \simeq (U, V, 1) + (\hat{u}, \hat{v}, \hat{h})(x, y, t), \tag{3.11}$$

into the abyssal current equations (2.36) and (2.37), assuming the bottom topography (3.2) and the steady solutions (3.7) and (3.8), gives, after linearizing with respect to the perturbation fields, dropping the carets and a little algebra,

$$(\partial_t + \boldsymbol{U} \cdot \nabla)u = \left[\frac{1}{R_e}\Delta - c_D\gamma(1 + \gamma^2 f^2)\right]u + f(1 - c_D^2\gamma^4)v + (c_D f\gamma^3 - \partial_x)h, \tag{3.12}$$

$$(\partial_t + \boldsymbol{U} \cdot \nabla)v = \left[\frac{1}{R_e}\Delta - c_D\gamma\left(1 + c_D^2\gamma^4\right)\right]v - f\left(1 + c_D^2\gamma^4\right)u + \left(c_D^2\gamma^4 - \partial_y\right)h, \tag{3.13}$$

$$(\partial_t + \boldsymbol{U} \cdot \nabla)h + \nabla \cdot \boldsymbol{u} = 0, \tag{3.14}$$

where $\boldsymbol{u} = (u, v)$. The linear stability equations for the upper layer are simply (2.31), (2.32) and (2.33).

3.2.1. *The inviscid and non-rotating stability problems*

Before turning to solving the general normal mode equations associated with (3.12), (3.13) and (3.14), it is instructive to examine two sublimits in the abyssal-layer stability equations. These will be quite useful in the interpretation of the more general rotating results.

In the absence of bottom friction (i.e. $c_D = 0$) there is no instability and the solutions to (3.12), (3.13) and (3.14) correspond to a superposition of linear internal gravity waves with horizontal dissipation present, superimposed on a constant-speed current. We expect, therefore, that rotation will be a stabilizing influence in the stability problem. That is, the rotation dominated situation is neutrally stable.

In the absence of rotation (i.e. $f = 0$), (3.12), (3.13) and (3.14) reduce to the governing equations for classical linear roll waves. Setting $f = \partial_x = u = U = 0$ and $V = \gamma = 1/\sqrt{c_D}$ (see (3.8)), eliminates the alongslope momentum equation (3.12), and (3.13) and (3.14) reduce to

$$\left(\partial_t + \frac{1}{\sqrt{c_D}}\partial_y\right) v = \left(\frac{1}{R_e}\partial_{yy} - 2\sqrt{c_D}\right) v + (1 - \partial_y)h,$$

$$\left(\partial_t + \frac{1}{\sqrt{c_D}}\partial_y\right) h + v_y = 0,$$

which can be combined together to give

$$\left[\left(\partial_t + \frac{1}{\sqrt{c_D}}\partial_y\right)^2 - \partial_{yy}\right] v + \left(2\sqrt{c_D} - \frac{1}{R_e}\partial_{yy}\right)\left(\partial_t + \frac{1}{\sqrt{c_D}}\partial_y\right) v + v_y = 0. \quad (3.15)$$

If we assume a normal mode solution to (3.15) of the form

$$v \sim \exp[i l y + (\sigma - i l/\sqrt{c_D})t] + \text{c.c.},$$

where l is the real-valued cross-slope wavenumber, $i^2 = -1$, σ is the complex-valued 'growth rate', and where c.c. means complex conjugate, we obtain the dispersion relationship

$$\sigma = -\left(\sqrt{c_D} + \frac{l^2}{2R_e}\right) \pm \sqrt{\left(\sqrt{c_D} + \frac{l^2}{2R_e}\right)^2 - (il + l^2)}. \quad (3.16)$$

A mode with a given cross-slope wavenumber l will be stable, i.e. $\text{Re}(\sigma) \leqslant 0$, provided

$$\text{Re}\left\{\sqrt{\left(\sqrt{c_D} + \frac{l^2}{2R_e}\right)^2 - (il + l^2)}\right\} \leqslant \sqrt{c_D} + \frac{l^2}{2R_e},$$

which is satisfied if and only if

$$\sqrt{c_D} + \frac{l^2}{2R_e} \geqslant \tfrac{1}{2}. \quad (3.17)$$

Thus, in the non-rotating limit,

$$c_D \geqslant \tfrac{1}{4} \iff \text{stability}, \quad (3.18)$$

which is just the classical roll-wave stability result (see, e.g. Jeffreys 1925; Whitham 1974; Baines 1995; Mandre 2001).

In addition, we note that (3.17) implies the existence of a high wavenumber cutoff if R_e is finite. Indeed, if R_e is infinite, then it can be shown that the instability problem
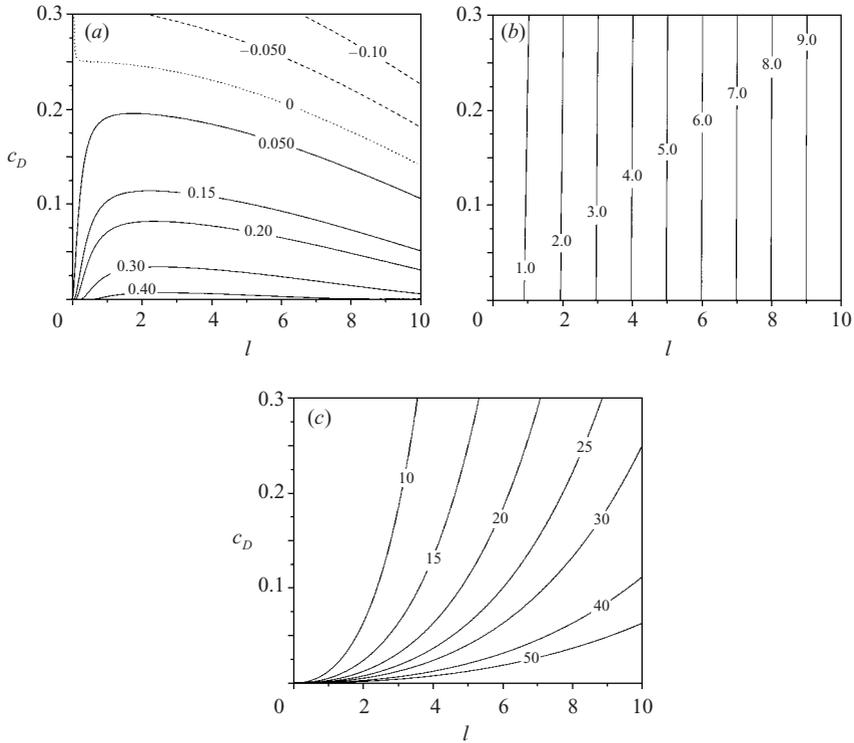
FIGURE 3. (*a*) Growth rate, (*b*) relative frequency and (*c*) geostationary frequency of the
max[Re(σ)] mode in the (l, c_D)-plane for $f = 0$.

exhibits an ultraviolet catastrophe in the sense that the most unstable mode has
an infinite wavenumber or zero horizontal wavelength. However, this is outside the
asymptotic assumptions upon which the shallow-water model for the abyssal current
is based, i.e. $h_*/L \ll 1$.

The necessary and sufficient instability condition

$$\frac{1}{c_D} > 4,$$

can be rewritten in terms of the Froude number. It follows from (3.10) that, in terms
of dimensional quantities, the instability condition is

$$F \equiv \frac{V^*}{\sqrt{g'h_*}} > 2,$$

so that instability occurs provided the downslope friction velocity is greater than
twice the internal gravity-wave speed (for the abyssal current in the reduced gravity
approximation), or, equivalently, the (non-rotating slope) Froude number is greater
than 2. Roll waves, therefore, can only form on a frictional overflow which is
sufficiently supercritical.

3.3. *The non-rotating instability*

3.3.1. *Spectral characteristics of the non-rotating instability*

Figure 3(*a*) is a contour graph of the maximum real part of $\sigma(l, c_D, R_e)$,
denoted by max[Re(σ)], as determined by (3.16) for $R_e = 400$ (we recall that

here $f = k = u = U = 0$) in the (l, c_D)-plane. We note that, in general, $\max[\mathrm{Re}(\sigma)]$ corresponds to the real part of the positive root in (3.16). We do not wish to call this the most unstable mode since it is more convenient and conventional to reserve that designation for the largest positive value of $\max[\mathrm{Re}(\sigma)]$ regarded as a function of the cross-slope wavenumber l (in the non-rotating limit). In the region where $\max[\mathrm{Re}(\sigma)] < 0$, i.e. the region of asymptotic stability, the contours are dashed. The stability boundary, i.e. the curve where $\max[\mathrm{Re}(\sigma)] = 0$, is dotted. The solid contours correspond to the region of instability, i.e. where $\max[\mathrm{Re}(\sigma)] > 0$.

Figure 3(a) seems to suggest that the highest growth rates would occur for $c_D = 0$. However, when $c_D = 0$, the friction velocity is infinite (see (3.10)). In this case, there is, in fact, no finite uniform steady solution and thus this situation is not physical. We must, therefore, interpret the growth rates obtained from (3.16) for $c_D \to 0$ as a limit in which the growth rate is, in fact, not defined at the limit point, i.e. it is discontinuous at $c_D = 0$. As we will show, this particular singularity does not occur when rotation is present. However, as we will show, this means that the non-rotating stability characteristics will form the singular limit of the rotating stability results.

Figure 3(b) is a contour plot of the relative frequency of the $\max[\mathrm{Re}(\sigma)]$ mode, as determined by (3.16), for $R_e = 400$, i.e. without rotation, in the (l, c_D)-plane. The 'relative frequency' is the frequency of the normal mode in a frame of reference moving with the mean abyssal current, i.e. it is simply $-\mathrm{Im}(\sigma)$ (see the form of the normal mode solution to (3.15)).

We can see that, in the non-rotating limit, the frequency is a slowly varying function of the bottom drag coefficient and appears to vary more or less linearly as a function of the cross-slope wavenumber l. The positive values of the frequency imply prograde phase propagation relative to the current, that is, the phase is moving in the downslope direction and the phase speed is larger than the mean abyssal current downslope speed.

Figure 3(c) is a contour plot of the geostationary frequency, i.e. the frequency in a geostationary frame of reference, of the $\max[\mathrm{Re}(\sigma)]$ mode, as determined by (3.16) for $R_e = 400$, i.e. without rotation, in the (l, c_D)-plane. The geostationary frequency is given by $l/\sqrt{c_D} - \mathrm{Im}(\sigma)$ (see the form of the normal mode solution to (3.15)). We see that the geostationary frequency depends quite sensitively on the cross-slope wavenumber l and bottom friction coefficient c_D. For a given cross-slope wavenumber, the geostationary frequency decreases with increasing bottom friction.

Figure 3(a) suggests that the most unstable mode occurs for a cross-slope wavenumber of between 2 and 3 for small values of the bottom drag coefficient with a trend to smaller wavenumbers as c_D increases. Of course, as c_D increases, the growth rate of the most unstable mode will decrease.

Figure 4(a) is a plot of the growth rate of the most unstable mode (denoted as $\mathrm{Re}(\sigma_{\max})$) versus the bottom drag coefficient c_D, for $R_e = 400.0$, as determined by (3.16). We recall that here $f = k = u = U = 0$. By most unstable mode we mean the largest value of $\max[\mathrm{Re}(\sigma)]$ when considered as a function of the cross-slope wavenumber l, for a given value of the parameters (c_D, R_e). That is, the most unstable mode satisfies $\partial\mathrm{Re}(\sigma)/\partial l = 0$. We denote the most unstable mode as $\sigma_{\max}$. The growth rate of the most unstable mode monotonically decreases as c_D increases until $c_D = 0.25$ is reached. After this point, the most unstable mode is neutrally stable. The singular nature of the limit point $c_D = 0$ is indicated with an open circle at that point.

Figure 4(b) is a plot of the cross-slope wavenumber of the most unstable mode (denoted as $l_{\max}$) versus the bottom drag coefficient c_D, for $R_e = 400$, as determined by (3.16). The cross-slope wavenumber of the most unstable mode monotonically
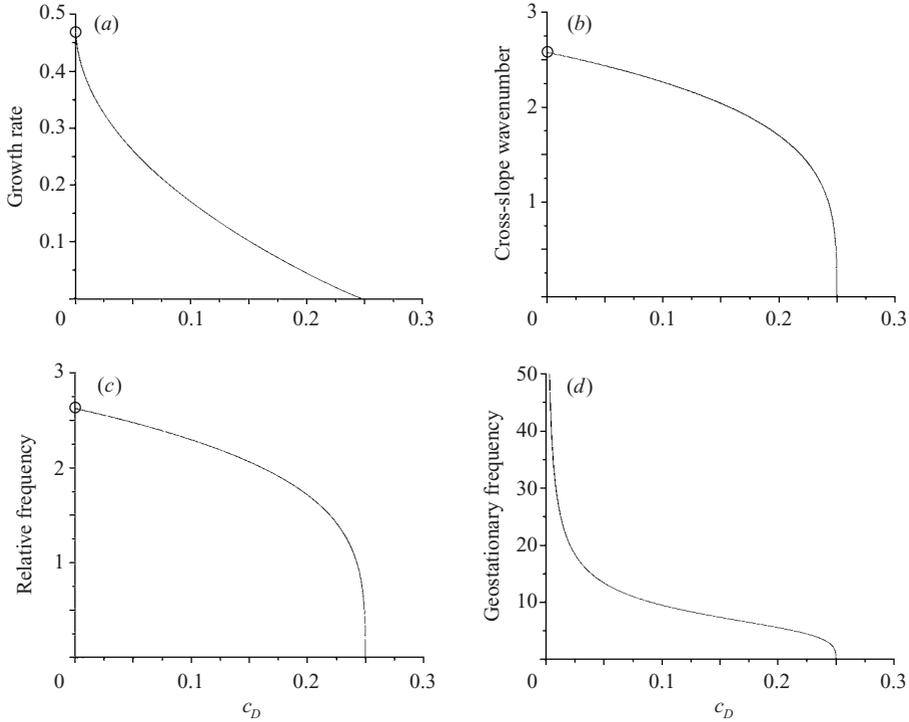
FIGURE 4. (a) $\text{Re}(\sigma_{max})$, (b) l_{max}, (c) ω^{rel}_{max} and (d) ω^{geo}_{max}, vs. c_D for $f = 0$.

decreases as c_D increases until $c_D = 0.25$ is reached. After this point the most unstable mode has a zero growth rate and has cross-slope wavenumber $l = 0$. As in figure 4(a), the singular nature of the limit point $c_D = 0$ is indicated with an open circle at that point.

In figure 3(b) we saw that the relative frequency of the $\max[\text{Re}(\sigma)]$ mode has, to leading order, approximately the same value as l. Thus, we expect that the curve of the relative frequency of the most unstable mode as a function of c_D, will be very similar to that shown in figure 4(b). Indeed, this can be seen in figure 4(c), where we plot the relative frequency of the most unstable mode (which we denote as $\omega^{ref}_{max} = -\text{Im}(\sigma_{max})$) versus c_D, for $R_e = 400$, as determined by (3.16). Figure 4(c) shows that at the point of marginal stability, i.e. $c_D = 0.25$, the relative frequency of the most unstable mode is zero when rotation is not present.

We therefore see that, in the non-rotating limit, marginally stable modes possess the principle of exchange of stabilities in a frame moving with the mean abyssal current (Drazin & Reid 1981). We will show that the principle of exchange of stabilities does not hold when rotation is introduced. In the geostationary frame, the frequency of the most unstable mode (which we denote as $\omega^{geo}_{max} = l/\sqrt{c_D} - \text{Im}(\sigma_{max})$) is infinite at $c_D = 0$ since the mean flow speed becomes unbounded (see figure 4(d)).

3.3.2. Internal gravity wave field for the non-rotating instability

The vertical structure of the internal gravity field in the overlying ocean, associated with the instabilities in the non-rotating limit, is determined by assuming a normal mode solution to (2.31), (2.32) and (2.33) of the form

$$\varphi = \psi(z)\exp[ily + (\sigma - il/\sqrt{c_D})t] + \text{c.c.},$$

where we recall that for the non-rotating limit $f = k = 0$ and $V = 1/\sqrt{c_D}$, yielding

$$\psi_{zz} - \left[\frac{l\sqrt{B}}{(\sigma - il/\sqrt{c_D})} \right]^2 \psi = 0, \tag{3.19}$$

subject to

$$\psi_z = 0 \quad \text{on} \quad z = 0, \tag{3.20}$$

$$\psi_z = -B \quad \text{on} \quad z = -1, \tag{3.21}$$

and where we have assumed, for convenience, a constant Burgers number (linear stratification in the overlying ocean) and set (without loss of generality) the normal mode amplitude of the perturbation abyssal current height to 1.0 (i.e. a positive height perturbation in the overflow thickness), respectively.

The solution to (3.19), (3.20) and (3.21) is simply

$$\psi(z) = \frac{(\sigma - il/\sqrt{c_D})\sqrt{B}\cosh[l\sqrt{B}z/(\sigma - il/\sqrt{c_D})]}{l\sinh[l\sqrt{B}/(\sigma - il/\sqrt{c_D})]},$$

which implies that the vertical structure in the (normal mode) vertical velocity will be described by (see (2.35))

$$
\begin{aligned}
w(z) &= \frac{(il/\sqrt{c_D} - \sigma)}{B}\psi_z \\
&= \frac{(il/\sqrt{c_D} - \sigma)\sinh[l\sqrt{B}z/(\sigma - il/\sqrt{c_D})]}{\sinh[l\sqrt{B}/(\sigma - il/\sqrt{c_D})]}.
\end{aligned}
\tag{3.22}
$$

In order to sketch the vertical structure, we need to assume values for the parameters. Suppose we set $c_D = 0.1$ and $R_e = 400.0$. The non-dimensional downslope velocity of the overflow current is approximately $V = 3.16$. The most unstable mode, for which we label the cross-slope wavenumber by l_{max} and the complex-valued growth rate by σ_{max}, occurs at approximately $l_{max} = 2.27$ (see figure 4b), has a real growth rate of approximately $\text{Re}(\sigma_{max}) = 0.17$ (see figure 4a), a relative frequency of approximately $-\text{Im}(\sigma_{max}) = 2.30$ (see figure 4c), and a geostationary frequency of approximately $Vl_{max} - \text{Im}(\sigma_{max}) = 9.46$ (see figure 4d).

These values imply an unscaled bottom friction parameter of $c_D^* = 0.002$ and a dimensional overflow velocity of approximately $180\,\text{cm s}^{-1}$, which are not inconsistent with, for example, observed near-sill values for the DSO (Spall & Price 1998; Käse *et al.* 2002). (When rotation is introduced the mean downslope velocity will be, as we will show, reduced to about $120\,\text{cm s}^{-1}$.) Dimensionally, the most unstable mode will have a cross-slope wavelength of about 14 km, will have a relative period of about 6 h, a geostationary period of about 1.5 h (this is the dramatic Doppler shift of the relatively rapid overflow), and e-folding growth time of about 13 h. Of course, these would also be the spectral characteristics of the internal gravity wave field in the overlying ocean associated with the instability.

Figure 5 is a plot of the real part of vertical structure function $w(z)$, as determined by (3.22), for the most unstable mode associated with $c_D = 0.1$ and $R_e = 400.0$, for a moderate and larger value of the Burgers number, respectively. We see that the excited internal gravity waves are bottom intensified. For moderate values of the Burgers number (e.g. $B \approx 1$ corresponding to $N \approx 0.01\,\text{s}^{-1}$), the vertical velocity falls off approximately linearly with vertical distance or height from the unstable overflow.

For larger values of the Burgers number (e.g. $B \approx 40$ corresponding to $N \approx 0.06\,\text{s}^{-1}$) the overlying fluid is, of course, more strongly stratified and the internal gravity waves
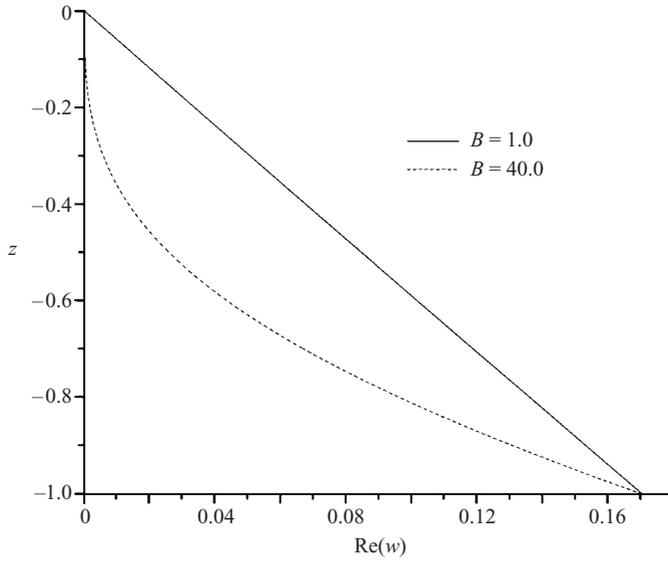
FIGURE 5. Vertical structure of the vertical velocity for $B = 1.0$ and 40.0.

are more effectively trapped near the overflow (see, also, Rhines 1970). The positive values of $\mathrm{Re}(w(z))$ are a reflection of the fact that (3.22) implicitly assumes an overflow perturbation thickness modal amplitude $h = 1.0$. However, for sufficiently large values of the Burgers number ($B \gtrsim 50$), it is possible to have a zero or nodal point in $\mathrm{Re}(w(z))$, so that there exists a near-surface region where $\mathrm{Re}(w(z)) < 0$ (although, of course, $w(0) = 0$).

3.4. *General normal mode stability equations*

The general normal mode stability problem is determined by substituting

$$(u, v, h) = (\tilde{u}, \tilde{v}, \tilde{h}) \exp[ikx + ily + (\sigma - ikU - ilV)t] + \text{c.c.}, \tag{3.23}$$

$$\varphi = \psi(z) \exp[ikx + ily + (\sigma - ikU - ilV)t] + \text{c.c.}, \tag{3.24}$$

into (2.31), (2.32), (2.33), (3.12), (3.13) and (3.14), giving

$$\psi_{zz} - \lambda^2 \psi = 0, \tag{3.25}$$

subject to

$$\psi_z = 0 \quad \text{on} \quad z = 0, \tag{3.26}$$

$$\psi_z = -Bh \quad \text{on} \quad z = -1, \tag{3.27}$$

with

$$\mathcal{M} [u, v, h]^\top = \mathbf{0}, \tag{3.28}$$

where we have assumed, for convenience, a constant Burgers number, dropped the tildes, and where

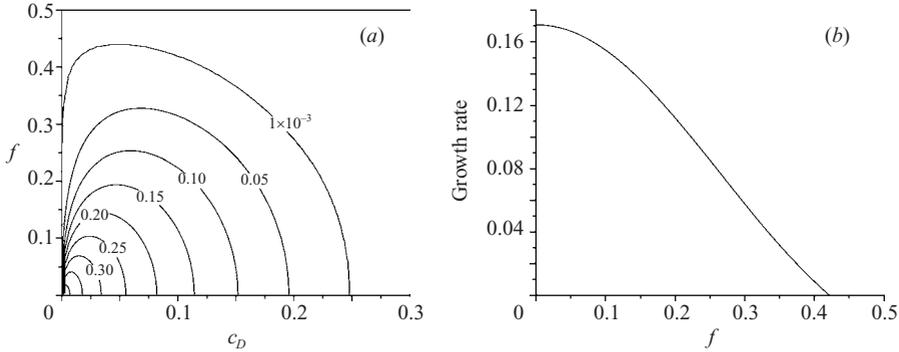$$\lambda^2 \equiv \frac{(k^2 + l^2)B}{(\sigma - ikU - ilV)^2 + f^2}, \tag{3.29}$$

FIGURE 6. (a) $\mathrm{Re}(\sigma_{\max})$ in the (c_D, f)-plane and (b) section along $c_D = 0.1$ in (a).

and $\mathcal{M}$ is the 3×3 matrix

$$
\mathcal{M} = \begin{bmatrix}
\sigma + \dfrac{k^2 + l^2}{R_e} + c_D \gamma (1 + \gamma^2 f^2) & f\left(c_D^2 \gamma^4 - 1\right) & ik - c_D f \gamma^3 \\[2mm]
f\left(1 + c_D^2 \gamma^4\right) & \sigma + \dfrac{k^2 + l^2}{R_e} + c_D \gamma \left(1 + c_D^2 \gamma^4\right) & il - c_D^2 \gamma^4 \\[2mm]
ik & il & \sigma
\end{bmatrix}.
$$

(3.30)

The vertical structure of the normal mode perturbations in the upper layer is determined by the solution to (3.25), (3.26) and (3.27), and is given by

$$
\psi(z) = \frac{Bh \cosh(\lambda z)}{\lambda \sinh(\lambda)},
$$

(3.31)

which implies that the vertical structure in the (normal mode) vertical velocity will be described by (see (2.35))

$$
\begin{aligned}
w(z) &= \frac{(ikU + ilV - \sigma)}{B} \psi_z \\
&= \frac{(ikU + ilV - \sigma)h \sinh(\lambda z)}{\sinh(\lambda)}.
\end{aligned}
$$

(3.32)

Equation (3.28) has non-trivial solutions if and only if

$$
\det \mathcal{M} = 0,
$$

(3.33)

which gives rise to a cubic polynomial in σ which can be solved to give solutions of the form

$$
\sigma = \sigma(c_D, f, R_e, k, l).
$$

(3.34)

Again, instability occurs if the growth rate $\mathrm{Re}(\sigma) > 0$.

4. Description of the instability with rotation and bottom friction

4.1. *Growth rate of the most unstable mode*

Figure 6(a) is a contour plot of the growth rate of the most unstable mode (denoted as $\mathrm{Re}(\sigma_{\max})$) in the (c_D, f)-plane assuming $R_e = 400.0$. The most unstable mode, denoted as $\sigma_{\max}$, is that normal mode with the largest value of $\mathrm{Re}(\sigma)$ considered as a function

of the wavenumbers (k, l) for a given value of the parameters (c_D, f, R_e). When instability occurs, the most unstable mode always occurs at a wavenumber vector $(k, l) = (k_{max}, l_{max})$ satisfying

$$\left.\frac{\partial \mathrm{Re}(\sigma)}{\partial k}\right|_{(k_{max}, l_{max})} = \left.\frac{\partial \mathrm{Re}(\sigma)}{\partial l}\right|_{(k_{max}, l_{max})} = 0, \\ \sigma_{max} = \sigma|_{(k_{max}, l_{max})}. \right\} \tag{4.1}$$

In figure 6(a) we can immediately see a number of properties associated with the instability as f increases (or, equivalently, as the Rossby number decreases). First, we note that figure 4(a) corresponds to the section in figure 6(a) along $f = 0$ (i.e. the c_D-axis). The sharp cutoff value for instability associated with the bottom friction coefficient continues to exist (but decreases) as f increases from zero. That is, instability continues to occur for $f > 0$, but does so for a smaller range of c_D values. In the non-rotating limit, the bottom friction coefficient cutoff value is given exactly by $c_D = 0.25$ (see (3.18) and figure 4(a)).

Although it is difficult to discern clearly in figure 6(a) (see figure 6b), there is a sharp boundary with respect to f, i.e. there is a distinct marginal stability curve, between the region of instability (where the growth rate is positive) and the region of stability (where the most unstable mode has zero growth rate, i.e. the abyssal flow is neutrally stable). The contour labelled 0.001 is very close to this boundary. (When we tried to contour the zero growth rate isoline exactly the contour package introduced a highly irregular multiply connected pattern.)

As f increases, figure 6(a) shows that the growth rate of the most unstable mode decreases monotonically. Nevertheless, figure 6(a) suggests that the frictional destabilization of abyssal overflows is possible for physically realizable values of f or, equivalently, the inverse Rossby number. For example, for $c_D = 0.1$ and $f = 0.25$ (i.e. a Rossby number of about 4.0), the most unstable mode has a (non-dimensional) growth rate of about 0.09 which corresponds to a (dimensional) e-folding time of about 24 h (this scales inversely with s^*, see §2.2). For $c_D = 0.1$ and $f = 0.25$, $U = 1.84$ and $V = 1.99$ which imply a dimensional along- and cross-slope velocity for the mean overflow of about $110 \, \mathrm{cm \, s^{-1}}$ and $120 \, \mathrm{cm \, s^{-1}}$, respectively.

Comparing figure 6(a) with figure 4(a), we can see how rotation eliminates the singular behaviour in the growth rate of the most unstable mode at $c_D = 0$ when rotation is present (i.e. $f > 0$). In figure 4(a) we marked this singularity by placing an open dot on the graph along $c_D = 0$. Although, formally, the limit of the growth rate of the most unstable mode as $c_D \to 0$ for $f = 0$ exists, there is, in fact, no solution to the linear stability problem since there is no bounded solution to the (U, V) mean flow equations (3.7) and (3.8) for $c_D = f = 0$. As a result, the entire stability calculation (and, indeed, the entire theory) presented here is meaningless at $c_D = f = 0$. However, if $f \neq 0$, there are bounded (U, V) mean flow solutions even if $c_D = 0$ (see (3.7) and (3.8)). Thus, the singularity at $c_D = 0$ is removed when rotation is present.

Nevertheless, in the rotating situation, if bottom friction is not present, there cannot be any frictional destabilization. This means that the growth rate of the most unstable mode for $c_D = 0$ if $f \neq 0$ must be no greater than zero. We can see this property in figure 6(a). The growth rate of the most unstable mode along the f-axis (with the origin excepted) is zero. Thus, for $f > 0$ (the same argument will hold in the southern hemisphere), the growth rate of the most unstable mode will increase as c_D initially increases from zero, reach a maximum value for a finite value of c_D, and then start to decrease until it equals zero at the bottom friction coefficient cutoff value (which
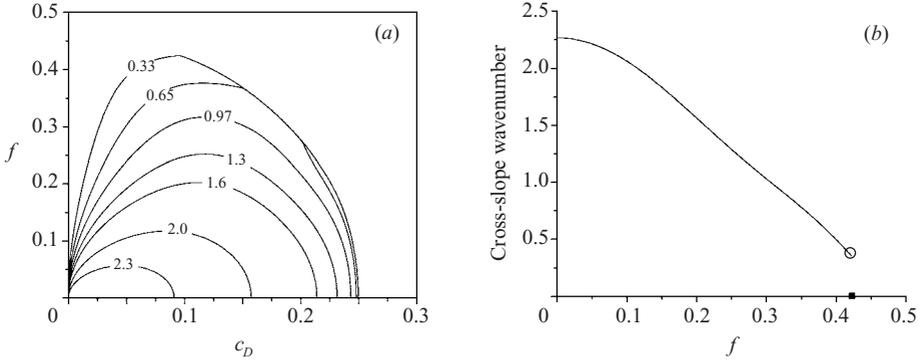
FIGURE 7. (a) l_{max} in the (c_D, f)-plane and (b) section along $c_D = 0.1$ in (a).

is less than or equal to 0.25). This behaviour is different from the strictly monotonic decrease in the growth rate of the most unstable mode as c_D increases from zero in the non-rotating case, as shown in figure 4(a).

Physically, the initial increase in the growth rate of the most unstable mode, when $f \neq 0$, as c_D initially increases from zero, occurs because the downslope velocity of the overflow is itself increasing for this region of increasing values of c_D. (It may, at first, seem counter-intuitive that increasing bottom drag can lead to increasing downslope velocity when rotation is present. The non-monotonic behaviour of the downslope velocity as a function of the bottom friction parameter when rotation is present has been previously discussed in this section). However, for sufficiently large values of the bottom friction coefficient, drag ultimately results in a decreasing downslope mean velocity, so that the growth rate of the most unstable mode will decrease until the bottom friction coefficient cutoff value is reached, after which the most unstable mode is neutrally stable.

Figure 6(b) is a graph of the growth rate of the most unstable mode, assuming $c_D = 0.1$ and $R_e = 400.0$, versus f (or inverse Rossby number). Figure 6(b) corresponds to the section in figure 6(a) along $c_D = 0.1$. We can see the monotonic decrease in the growth rate of the most unstable mode as f increases and the sharp stability boundary (i.e. the slope of the growth rate curve is discontinuous at the point of marginal stability) located at about $f \approx 0.42$ for $c_D = 0.1$.

4.2. *Downslope and alongslope wavenumber of the most unstable mode*

Figure 7(a) is a contour plot of the cross-slope (l_{max}) wavenumber of the most unstable mode in the (c_D, f)-plane for $R_e = 400.0$. Figure 4(b) corresponds to the section in figure 7(a) along $f = 0$ (i.e. the c_D axis).

Examining figure 7(a) (see also figure 7b) we see that l_{max} decreases, for a given value of c_D, as f increases. Along the f-axis, away from $f = 0$, $l_{max} = 0$ in figure 7(a), since there is no instability when $c_D = 0$. However, unlike in the non-rotating situation (see figure 4b), the limit of l_{max}, as we approach the point of marginal stability from within the region of instability, is not zero (see figure 7b). This means that across the 'interior' marginal stability boundary in the (c_D, f)-plane, i.e. the stability boundary away from the axes, the cross-slope and (as we will show) alongslope wavenumbers and the frequency of the most unstable mode will be discontinuous. Rotation, therefore, has removed the singularity along $c_D = 0$ ($f > 0$), only to introduce another singularity elsewhere in the (c_D, f)-plane.
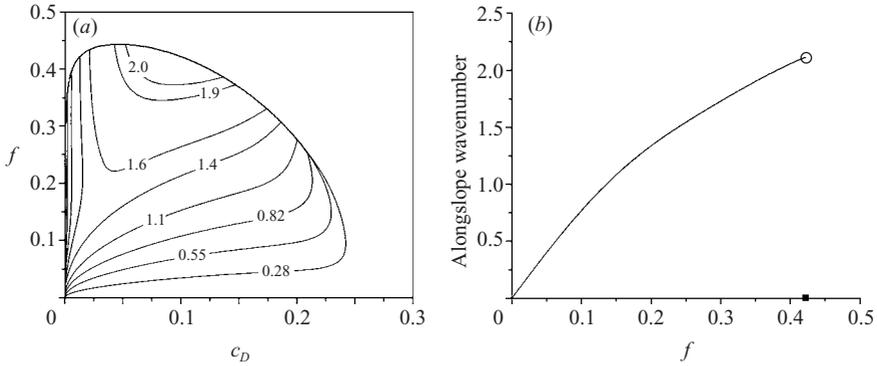
FIGURE 8. (a) k_{max} in the (c_D, f)-plane and (b) section along $c_D = 0.1$ in (a).

In figure 7(b), which corresponds to the section in figure 7(a) along $c_D = 0.1$, we show this discontinuity by placing an open round dot at the limit value of l_{max}, as it would be determined from within the region of instability, and placed a solid square dot at the point of marginal stability at about $f \approx 0.42$ (where the flow is stable). We note that $l_{max} = 0$ for $f \gtrsim 0.42$ (in the stable region) in figure 7(b).

The reason that l_{max} (in fact, both l_{max} and k_{max}) will be zero in the region of stability, but away from the marginal stability boundary, is a consequence of the presence of horizontal friction in the linear stability problem (3.12), (3.13) and (3.14). The most unstable mode in the region of stability, when horizontal friction is present (which is proportional to the Laplacian operator), occurs when the magnitude of the wavenumber vector is zero since any other wavenumber pair will necessarily result in a more negative growth rate, when all other parameters are held constant.

As we have previously discussed, the overflow is neutrally stable along the f-axis, away from $f = 0$. As a result, $l_{max} = 0$ along the f-axis, away from $f = 0$. Hence, unlike in the non-rotating case (see figure 4b) where l_{max} monotonically decreases as c_D increases from zero until the stability boundary is reached, in the rotating case, l_{max} initially increases as c_D increases initially away from zero, reaches a maximum, and then decreases until c_D reaches its cutoff value associated with the given non-zero value of f. This is the pattern seen in figure 7(a).

It is useful to give a dimensional estimate of l_{max} in the rotating situation. If we consider $c_D = 0.1$ and $f = 0.25$, we find (see figure 7b) that $l_{max} \approx 1.29$, which implies a dimensional cross-slope wavelength of about 24 km. Of course, this wavelength would decrease as f decreases, until we reach the non-rotating limit (see figure 4b) of about 14 km (for $c_D = 0.1$). As rotation becomes more important in the dynamics, i.e. as f increases, the mean flow is progressively more aligned in the alongslope direction, and l_{max} decreases until the point of marginal stability is reached after which it is zero.

Figure 8(a) is a contour plot of the alongslope (k_{max}) wavenumber of the most unstable mode in the (c_D, f)-plane for $R_e = 400.0$. There is no (figure 4 series) plot corresponding to an $f = 0$ section for figure 8(a) since in the non-rotating limit $k = 0$. Indeed, figure 8(a) provides *a posteriori* justification for assuming, as we did, that we can set $k = 0$ in the non-rotating linear stability equations (see the derivation of (3.15)) since in the limit $f \to 0$, for $c_D > 0$, we see that $k_{max} \to 0$.

For a given non-zero c_D, we see that as f increases from zero, k_{max} increases as well (see also figure 8b). Thus, as expected, as rotation becomes relatively more important in the dynamics, the cross-slope and alongslope wavelengths of the most
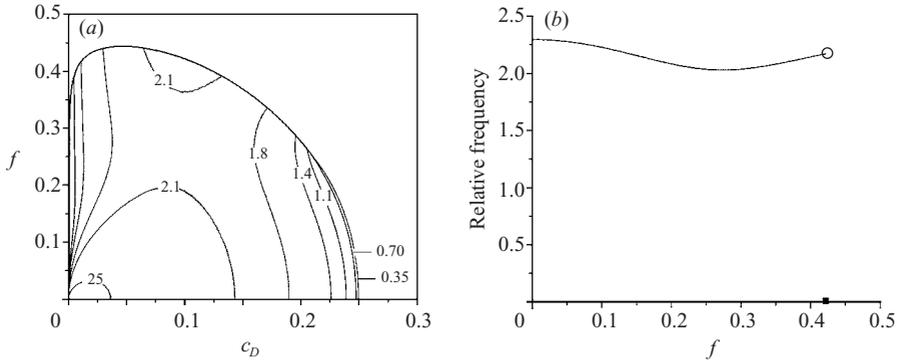
FIGURE 9. (a) $\omega_{\max}^{rel}$ in the (c_D, f)-plane and (b) section along $c_D = 0.1$ in (a).

unstable mode in the region of instability, decrease and increase, respectively, as the underlying flow becomes increasingly geostrophically adjusted and aligned in the alongslope direction.

Along the f-axis, away from $f = 0$, $k_{\max} = 0$ in figure 8(a), since there is no frictional instability when $c_D = 0$. Thus, $k_{\max}$ increases from zero as c_D increases from zero for $f > 0$. As in our discussion of $l_{\max}$, the interior marginal stability boundary forms a discontinuity in figure 8(a). In figure 8(b), which corresponds to the section in figure 8(a) along $c_D = 0.1$, we mark this discontinuity by placing an open round dot at the limit value of the cross-slope number as it would be determined within the region of instability, and place a solid square dot at the point of marginal stability at about $f \approx 0.42$ (where the flow is stable). Thus, $k_{\max} = 0$ for $f \gtrsim 0.42$ (in the stable region).

In figure 8(a), the maximum value of $k_{\max}$ is about 2.13 and occurs for (c_D, f) approximately given by $(0.1, 0.42)$, which corresponds to an interior limit value on the marginal stability boundary. For $c_D = 0.1$ and $f = 0.25$, we find (see figure 8b) that $k_{\max} \approx 1.55$, which implies a dimensional alongslope wavelength of about 20 km. This value for $k_{\max}$, together with our previous estimate for $l_{\max}$, implies a total dimensional wavelength of about $10\pi/\sqrt{k_{\max}^2 + l_{\max}^2} \approx 31$ km (see (2.30)) for the most unstable mode associated with $c_D = 0.1$ and $f = 0.25$.

4.3. *Frequency of the most unstable mode*

Figure 9(a) is a contour plot of the relative (that is, in a reference frame moving with the mean abyssal current) frequency of the most unstable mode, given by

$$\omega_{\max}^{rel} = -\text{Im}(\sigma_{\max}),$$

in the (c_D, f)-plane for $R_e = 400.0$. Figure 9(b) corresponds to the section in figure 9(a) along $c_D = 0.1$. figure 4(c) corresponds to the section in figure 9(a) along $f = 0$ (i.e. the c_D-axis). We note that positive values of $\omega_{\max}^{rel}$ imply prograde phase propagation with respect to the mean abyssal current. In figure 9(a), along the f-axis, away from $f = 0$, we see that $\omega_{\max}^{rel} = 0$ (because $l_{\max} = k_{\max} = 0$).

In figure 4(c), we saw that $\omega_{\max}^{rel}$, for $f = 0$, decreased as c_D increased. In figure 9(a), we see that this pattern holds when rotation is included. However, we see in figure 9(a), that there is comparatively little variation in $\omega_{\max}^{rel}$ with respect to f for fixed c_D. This can be clearly seen in figure 9(b). We have denoted the discontinuous
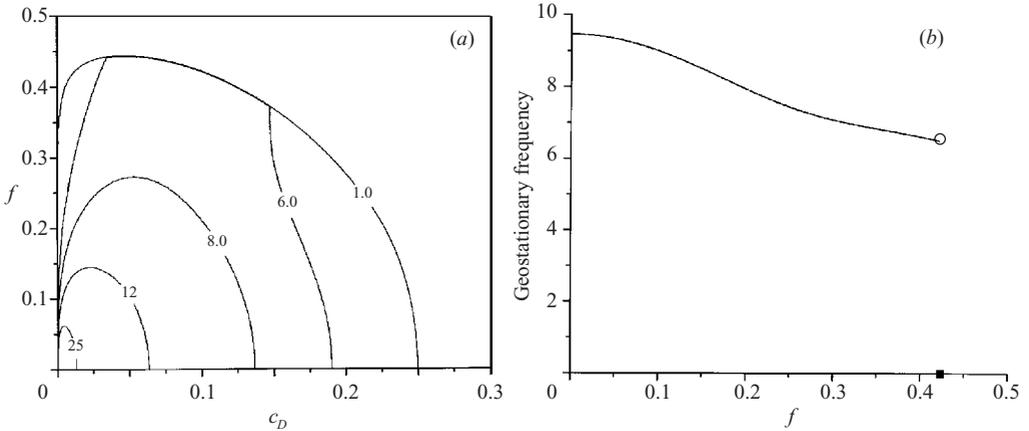
FIGURE 10. (a) ω_{max}^{geo} in the (c_D, f)-plane and section along $c_D = 0.1$ in (a).

behaviour of ω_{max}^{rel}, in figure 9(b), at the point of marginal stability, in the same manner as in figure 7(b). If we consider $c_D = 0.1$ and $f = 0.25$, we find (see figure 9b) that $\omega_{max}^{rel} \approx 2.04$, which implies a dimensional relative period of about 7 h. This is the period of the most unstable mode as it would be measured by an instrument drifting with the mean abyssal current.

Figure 10(a) is a contour plot of the geostationary frequency of the most unstable mode, given by

$$\omega_{max}^{geo} = U k_{max} + V l_{max} - \text{Im}(\sigma_{max}),$$

in the (c_D, f)-plane for $R_e = 400.0$. Figure 10(b) corresponds to the section in figure 10(a) along $c_D = 0.1$. Figure 4(d) corresponds to the section in figure 10(a) along $f = 0$ (i.e. the c_D-axis). While the relative frequency results are useful for understanding the propagation characteristics of the unstable modes in a reference frame moving with the mean overflow current, the geostationary representation is, perhaps, the more natural way to view the stability results since this would be the reference frame of observations taken from bottom-moored instruments.

Comparing figure 10(a) with figure 9(a), and figure 10(b) with figure 9(b), respectively, we can see the dramatic Doppler shift of these relatively rapid overflows. Nevertheless, as f increases, away from $c_D = 0$ (the f-axis), we see the general trend to lower, yet not subinertial, frequencies. Again, along the f-axis in figure 10(a), away from $f = 0$, $\omega_{max}^{geo} = 0$ (because $l_{max} = k_{max} = 0$). If we consider $c_D = 0.1$ and $f = 0.25$, we find (see figure 10b) that $\omega_{max}^{geo} \approx 7.45$, which implies a dimensional geostationary period of about 2 h.

Thus, in summary, for $c_D = 0.1$ and $f = 0.25$, we would measure a most unstable mode with a geostationary period of about 2 h, a total wavelength of about 31 km and a e-folding growth time of about a day. The direction of phase propagation is in the down and along (in a right-handed sense) slope direction. For smaller f (larger Rossby number) or c_D (but still within the region of instability), the spectral characteristics are, in general, red-shifted toward longer alongslope wavelengths and periods, blue-shifted toward shorter cross-slope wavelengths and toward higher growth rates and hence toward more rapidly growing instabilities.
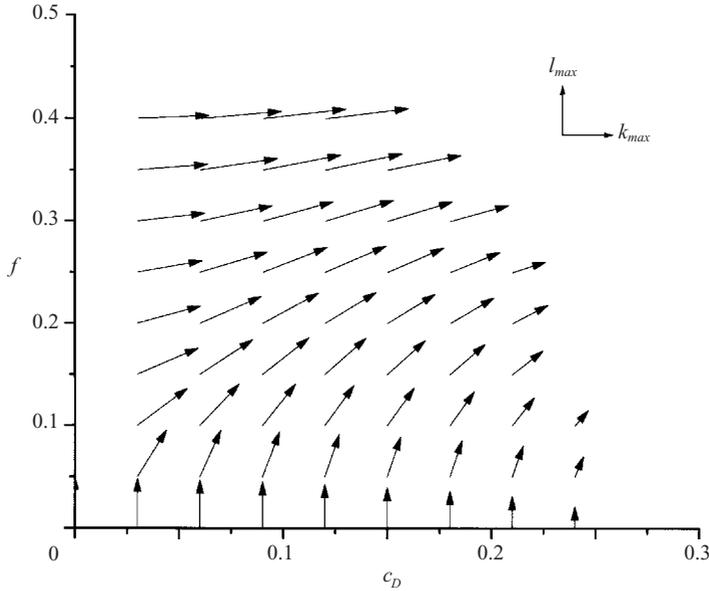
FIGURE 11. $(k_{\max}, l_{\max})$ in the (c_D, f)-plane.

4.4. *Internal gravity wave field in the overlying water*

The spectral characteristics $(k_{\max}, l_{\max})$ and $\sigma_{\max}$ will also be the horizontal wavenumbers and complex-valued growth rate of the internal gravity wave field in the overlying ocean generated by the instability. The vertical structure, or the z-dependence, of the vertical velocity is given by (3.32). Regardless or whether rotation is included or not, $w(z)$ will look very similar to that shown in figure 5 and so we do not present an additional plot with $f \neq 0$. With respect to the direction of phase propagation, increasing rotation will lead to the internal gravity wave field becoming progressively more aligned in the alongslope direction (since $k_{\max}$ increases and $l_{\max}$ decreases as f increases).

Figure 11 is a vector plot of the wavenumber vector $(k_{\max}, l_{\max})$ as a function of the bottom friction coefficient c_D and the non-dimensional Coriolis parameter f for the range $0 \leqslant c_D \leqslant 0.3$ and $0 \leqslant f \leqslant 0.5$. In order to ensure that the vectors remain within the plot boundaries, the velocity vectors have been scaled so that the length of the wavenumber vector located at $c_D = f = 0$ in figure 11 (located at the lower left-hand corner), has length 0.05 (its actual length is about 2.58, see figure 4b). We also remark that the vector located at $c_D = f = 0$ is, in fact, the limiting wavenumber vector obtained for $(k_{\max}, l_{\max})$ from within the region of instability (i.e. $c_D \to 0$ with $f = 0$, see figure 4b).

The wavenumber vectors are oriented so that positive $l_{\max}$ is indicated by the vector pointing in the direction of increasing f. Positive $k_{\max}$ is indicated by the vector pointing in the direction of increasing c_D. The orientation is shown in the upper right-hand corner in figure 11 by a $(k_{\max}, l_{\max})$ coordinate axes. The region of stability in the (c_D, f)-plane has no wavenumber vector shown because $(k_{\max}, l_{\max}) = \mathbf{0}$ there. We can see the general trend for the increasing orientation toward alongslope propagation as f increases for a given c_D. In addition, we can see the general trend of diminishing $k_{\max}$ as c_D increases for a given f as well as an overall decrease in the magnitude of the wavenumber vector (i.e. a trend to longer waves).
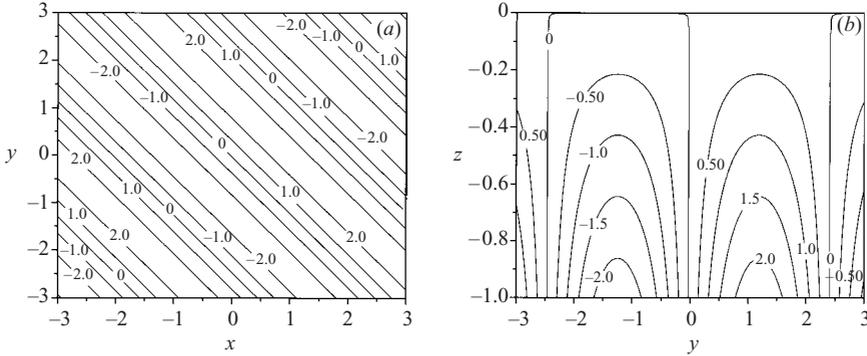
FIGURE 12. (a) $w(x, y, -1, 0)$ in the (x, y)-plane and (b) $w(0, y, z, 0)$ in the (y, z)-plane.

Figure 12(a) is a contour plot of a horizontal section of the total vertical velocity in the overlying ocean, given by,

$$w(x, y, z, t) = \mathrm{Re} \left\{ \frac{(\mathrm{i}kU + \mathrm{i}lV - \sigma)h \sinh(\lambda z)}{\sinh(\lambda)} \exp[\mathrm{i}kx + \mathrm{i}ly + (\sigma - \mathrm{i}kU - \mathrm{i}lV)t] \right\},$$

with $z = -1$ (immediately above the abyssal overflow), $t = 0$, $B = 1$ and $h = 1$ (for convenience) for the most unstable mode

$$\sigma_{max} \approx 0.09 - 2.04\mathrm{i}, \quad k_{max} \approx 1.55, \, l_{max} \approx 1.29,$$

$$U \approx 1.84, \quad V \approx 1.99,$$

for $c_D = 0.1$ and $f = 0.25$. We recall that the bottom topography is given by $h_B = -y$ (see (3.2)) so that the depth increases with increasing y. The wave field propagates from the lower left-hand corner toward the upper right-hand corner.

From (2.15), (2.29) and (2.30), the scale vertical velocity will be about $1.2 \, \mathrm{cm \, s^{-1}}$. Thus, assuming a non-dimensional perturbation thickness in the abyssal current of about 0.1 (corresponding to about a dimensional abyssal current height anomaly of about 10 m), Figure 12(a) suggests a dimensional vertical velocity in the overlying water column, immediately above the abyssal current, associated with the generated internal gravity wave field of about $0.25 \, \mathrm{cm \, s^{-1}}$. We note again that figure 12(a) assumes that $h = 1$, so that $h = 0.1$ would reduce the w values by a factor of 10.

Figure 12(b) is a contour plot of a vertical section of the total vertical velocity in the overlying ocean along $y = 0$ with $t = 0$ and $h = 1$ (again, for convenience) for the most unstable mode for $c_D = 0.1$ and $f = 0.25$. We can see the bottom intensification in the internal wave field and, for $B = 1$ (see figure 5), the linear decrease in the magnitude of w with decreasing depth. For larger values of B (see figure 5), the internal gravity wave field is increasingly bottom intensified.

4.5. Effect of variations in the parameters

The bottom slope parameter s^* is not explicitly present in the dispersion relationship (3.33) or (3.34). The bottom slope parameter is explicitly used in the definitions of the Reynolds number R_e, the non-dimensional Coriolis parameter (or inverse Rossby number) f and the scaled bottom friction parameter c_D as described by (2.25). All three parameters depend inversely on s^*. There is, however, another effect of variations in the bottom slope and that is on the time scale $T = \sqrt{h_*/g'}/s^*$ and horizontal length scale $L = h_*/s^*$ which also both depend inversely on s^*.

Thus, increasing s^* will lead to decreasing c_D and f and from figure 6(a) we see that this will, in general, lead to an increase in the non-dimensional growth rate and hence reduce the non-dimensional e-folding growth time. In addition, the associated decrease in the time scale T will act to further decrease the already reduced dimensional e-folding growth time. There will be a compounding of the two effects.

On the other hand, with respect to the effect that variations in the bottom slope parameter have on the wavelength of the most unstable mode, the situation is a little more complicated. From figures 7(a) and 8(a), we see that increasing s^* will, in general, imply that l_{max} and k_{max} will increase and decrease, respectively. The increase in l_{max} and the decrease in L, for increasing s^*, reinforce each other and will lead to a decreasing dimensional cross-slope wavenumber for the most unstable mode. We cannot be so definitive about the alongslope wavenumber since the effect of increasing s^* on k_{max} and L (both will decrease) will oppose each other.

With respect to the frequency of the most unstable mode, figures 8(a) and 9(a) suggest that both the relative and geostationary frequencies will increase as the bottom slope increases. This effect will compound with the decreasing time scale to imply that the relative and geostationary dimensional periods of the most unstable mode will decrease for increasing s^*.

For example, if $c_D = 0.05$ and $f = 0.125$ (corresponding to a doubling of the bottom slope parameter as compared to that assumed for $c_D = 0.1$ and $f = 0.25$ when all other parameters are held constant), we find that (assuming $R_e = 400.0$) the most unstable mode has $\mathrm{Re}(\sigma_{max}) \approx 0.21$, $l_{max} \approx 1.85$, $k_{max} \approx 1.21$, $\omega_{max}^{ref} \approx 2.24$ and $\omega_{max}^{geo} \approx 11.38$. With respect to the underlying time and length scales, doubling the bottom slope parameter will lead to $T \approx 1.1\,\mathrm{h}$ and $L \approx 2.5\,\mathrm{km}$ (holding g' and h_* fixed). Thus, we find that for $c_D = 0.05$ and $f = 0.125$, the most unstable mode will have a dimensional e-folding growth time of about 5.24 h, a cross-slope wavelength of about 8.5 km and an alongslope wavelength of about 13 km (for a total wavelength of about 15 km), a relative period of about 3.1 h and geostationary period of about 36 min (the dimensional cross-slope and downslope mean abyssal current velocities will be about 120 and a rather large 212 cm s^{-1}, respectively).

Within the context of a finite R_e, variations in R_e will lead to only quantitative changes in the description given here. The existence of the stability boundaries as shown in figures 7–10 will not change, but the value of the limiting wavenumbers and frequency as we approach the marginal stability boundary from within the region of instability will change. For a given value of the other parameters, increasing (but finite) R_e will lead to only modest increases in the growth rate of the most unstable mode. This is a consequence of the fact that l_{max} and k_{max} remain $O(1)$. Perhaps the most fundamental aspect of the stability characteristics associated with a finite Reynolds number is the existence of a high wavenumber cutoff for instability (which is inversely related to R_e (see (3.17) when $f = 0$). Thus, for increasing (but finite) R_e, we expect a shift to higher wavenumbers for the most unstable mode. For example, if we set $R_e = 4000$ (a tenfold increase) but keep $c_D = 0.1$ and $f = 0.25$, we find that the most unstable mode has $\mathrm{Re}(\sigma_{max}) \approx 0.093$, $l_{max} \approx 2.71$, $k_{max} \approx 2.73$, $\omega_{max}^{ref} \approx 3.86$ and $\omega_{max}^{geo} \approx 14.29$.

The remaining two parameters relevant to the instability are g' and h_*. Neither of these parameters appears explicitly in the stability problem. Variations in g' and h_* will lead to variations in f, R_e, L and T, but leaves c_D unchanged. Perhaps the most straightforward way to understand the effect of the variations in these two parameters is to remind ourselves that the underlying reason for the destabilization is that the downslope frictional velocity is sufficiently supercritical with respect to the speed of

long internal gravity waves. When g' and h_* increase, all else being constant, the speed of long internal gravity waves within the abyssal current increases (since it is given by $\sqrt{g'h_*}$). Thus, for a given downslope abyssal current velocity, increasing g' and h_* will mean that the Froude number will decrease and this will have a stabilizing effect.

5. Conclusions

A simple model has been introduced to examine the stability characteristics of frictionally destabilized abyssal overflows and to determined the structure of the internal gravity wave field in the surrounding ocean associated with the instability. The possibility that abyssal overflows can be destabilized by bottom friction is suggested by both oceanographic observations and numerical simulations which indicate that overflow speeds are comparable to the phase/group velocity of long internal gravity waves within the abyssal current itself.

Our model development began with a two-layer geometry in which the layer overlying the abyssal current could be initially described by the adiabatic Boussinesq equations for a continuously stratified rotating fluid. It was assumed that the abyssal layer could be described by the shallow-water equations for a homogeneous fluid with horizontal and bottom friction present as well as variable bottom topography.

We then presented a scaling argument which suggested that while the overlying layer could be modelled, to leading order, by the linear long-wave equations for a stratified rotating fluid, the abyssal layer is described by the full nonlinear shallow-water equations with rotation, downslope gravitational acceleration and horizontal and bottom friction present. To leading order, there is no two-way dynamic coupling between the two layers. However, motion in the upper layer is forced by horizontal mass convergence/divergence created by vertical motion in the interface between the two layers.

We show that the non-dimensional stability problem is naturally studied in terms of a scaled bottom friction parameter (which is equivalent to the inverse non-rotating Froude number) and a scaled Coriolis parameter (which is equivalent to the inverse temporal Rossby number). The stability characteristics are principally determined by these two parameters with the Burgers number for the overlying ocean and the Reynolds number within the abyssal layer playing secondary (but important) roles.

We began our stability calculation by finding the general form of steady 'slab' solutions to the abyssal-layer equations and determined their dependence on the (scaled) bottom friction and Coriolis parameters. The non-rotating stability problem can be solved exactly. In particular, we showed that in the non-rotating limit, our results recover the well-known dispersion relation for classical roll waves. The structure of the internal gravity waves in the overlying fluid for the non-rotating stability problem was described. These solutions were quite useful in describing the role that rotation plays in the stability problem.

We then turned to examining the full stability problem with rotation included. We showed that while, as expected, rotation acts as a stabilization influence in an otherwise unstable supercritical abyssal overflow, frictional destabilization was still possible for physically accessible values of the non-dimensional Coriolis parameter (or inverse Rossby number). In addition, as expected, rotation acts to orient the direction of phase propagation, of the most unstable mode, increasingly in the alongslope direction.

Although, clearly dependent on the value of the physical parameters, the theory presented here suggests a most unstable mode with a 'typical' geostationary period of about 2 h, a total wavelength of about 31 km and an *e*-folding growth time of about a day. The internal gravity wave field generated in the overlying water column is attenuated with height from the abyssal current with the attenuation increasing as the Burgers number increases. Typical vertical velocities associated with the internal gravity waves can be of the order of $0.25\,\mathrm{cm\,s^{-1}}$ immediately above the unstable abyssal overflow. The direction of phase propagation is in the down and along (in a right-handed sense) slope direction.

For larger Rossby number or smaller bottom friction coefficient (but still within the region of instability), the spectral characteristics are, in general, red-shifted toward longer alongslope wavelengths and periods, blue-shifted toward shorter cross-slope wavelengths and toward higher growth rates and hence correspond to more rapidly growing instabilities. Unlike the baroclinic instability theory described by Swaters (1991), which is subinertial, the destabilization described here connects overflow variability to superinertial long internal gravity waves.

We do not suggest that the frictional destabilization described here is responsible, in and of itself, for the observed mesoscale cyclogenesis in overflows. However, our work here does show that it is possible that frictional destabilization can occur in sufficiently rapid abyssal overflows in the near-sill region, perhaps prior to the full geostrophic adjustment of the overflow.

Further, we speculate that this instability may have a role to play in the observed rapid entrainment of ambient overlying water during the initial stages of overflow development. This latter possibility will be enhanced by the finite-amplitude development of the instabilities described here since, as is well known, the perturbations will grow into pulses or bores which ultimately break. The exploration of the nonlinear development of frictionally destabilized overflows will presumably require a numerical treatment. There is also the possibility that marginally unstable modes excited by the mechanism described here could resonantly interact with vortical modes, thereby funnelling energy into the subinertial range through nonlinear wave–wave interactions.

However, there still remains another mechanism which could possibly contribute to entrainment and mixing in overflows and which could act on superinertial time scales. Kelvin–Helmholtz instability is possible within overflows and this process has not, to our knowledge, been explored in this context before. It would be interesting to compare and contrast all three mechanisms.

REFERENCES

BAINES, P. G. 1995 *Topographic Effects in Stratified Flows.* Cambridge University Press.

BRUCE, J. G. 1995 Eddies southwest of Denmark Strait. *Deep-Sea Res.* **42**, 13–29.

CHOBOTER, P. F. & SWATERS, G. E. 2000 On the baroclinic instability of axisymmetric rotating gravity currents with bottom slope. *J. Fluid Mech.* **408**, 149–177.

DICKSON, R. R. & BROWN, J. 1994 The production of North Atlantic deep water: sources, rates, and pathways. *J. Geophys. Res.* **99**, 12 319–12 341.

DRAZIN, P. G. & REID, W. H. 1981 *Hydrodynamic Stability.* Cambridge University Press.

EMMS, P. W. 1998 A streamtube model of rotating turbidity currents. *J. Mar. Res.* **56**, 41–74.

ETLING, D., GELHARDT, F., SCHRADER, U., BRENNECKE, F., KÜHN, G., CHABERT D'HIERES, G. & DIDELLE, H. 2000 Experiments with density currents on a sloping bottom in a rotating fluid. *Dyn. Atmos. Oceans* **31**, 139–164.

GIRTON, J. B. & SANFORD, T. B. 2001 Synoptic sections of the Denmark Strait overflow. *Geophys. Res. Lett.* **28**, 1619–1622.

GIRTON, J. B. & SANFORD, T. B. 2002 Descent and modification of the Denmark Strait overflow. *J. Phys. Oceanogr.* (submitted).

HOUGHTON, R. W., SCHLITZ, R., BEARDSLEY, R. C., BUTMAN, B. & CHAMBERLIN, J. L. 1982 The middle Atlantic Bight cold pool: evolution of the temperature structure during summer 1979. *J. Phys. Oceanogr.* **12**, 1019–1029.

JEFFREYS, H. 1925 The flow of water in an inclined channel of rectangular bottom. *Phil. Mag.* **49**, 793–807.

JIANG, L. & GARWOOD, R. W. 1996 Three-dimensional simulations of overflows on continental slopes. *J. Phys. Oceanogr.* **26**, 1214–1233.

JUNGCLAUS, J. H., HAUSER, J. & KÄSE, R. H. 2001 Cyclogenesis in the Denmark Strait overflow plume. *J. Phys. Oceanogr.* **31**, 3214–3228.

KARSTEN, R. H. & SWATERS, G. E. 2000 Nonlinear effects in two-layer large-amplitude geostrophic dynamics. Part 2. The weak-beta case. *J. Fluid Mech.* **412**, 161–196.

KARSTEN, R. H., SWATERS, G. E. & THOMSON, R. E. 1995 Stability characteristics of deep water replacement in the Strait of Georgia. *J. Phys. Oceanogr.* **25** 2391–2403.

KÄSE, R. H., GIRTON, J. B. & SANFORD, T. B. 2002 Structure and variability of the Denmark Strait overflow: model and observations. *J. Geophys. Res.* (submitted).

KÄSE, R. H. & OSCHLIES, A. 2000 Flow through Denmark Strait. *J. Geophys. Res.* **105**, 28 527–28 546.

KILLWORTH, P. D. 1977 Mixing on the Weddell Sea continental slope. *Deep-Sea Res.* **24**, 427–448.

KRANENBURG, C. 1992 On the evolution of role waves. *J. Fluid Mech.* **245**, 249–261.

KRAUSS, W. 1996 A note on overflow eddies. *Deep-Sea Res.* **43**, 1661–1667.

KRAUSS, W. & KÄSE, R. H. 1998 Eddy formation in the Denmark Strait overflow. *J. Geophys. Res.* **103**, 15 523–15 538.

LANE-SERFF, G. F. & BAINES, P. G. 1998 Eddy formation by dense flows on slopes in a rotating fluid. *J. Fluid Mech.* **363**, 229–253.

LEBLOND, P. H., MA, H., DOHERTY, F. & POND, S. 1991 Deep and intermediate water replacement in the Strait of Georgia. *Atmos. Ocean* **29**, 288–312.

LEBLOND, P. H. & MYSAK, L. A. 1978 *Waves in the Ocean.* Elsevier.

MANDRE, S. 2001 Effect of bottom topography on roll wave instability. *Conceptual Models of the Climate. 2001 Summer Study Program in Geophysical Fluid Dynamics*, pp. 278–294. Woods Hole Oceanographic Institution.

MASSON, D. 2002 Deep water renewal in the Strait of Georgia. *Estuarine, Coastal Shelf Sci.* **54**, 115–126.

NEEDHAM, D. J. & MERKIN, J. H. 1984 On roll waves down an inclined channel. *Proc. R. Soc. Lond.* A **394**, 259–278.

NOF, D. 1981 The translation of isolated cold eddies on a sloping bottom. *Deep-Sea Res.* **30**, 171–182.

NOVIK, O. B. 1971 Model description of role waves. *Z. Angew. Math. Mech.* **35**, 938–951.

PEDLOSKY, J. 1997 *Geophysical Fluid Dynamics.* Springer.

POULIN, F. J. & SWATERS, G. E. 1999 subinertial dynamics of density-driven flows in a continuously stratified fluid on a sloping bottom. I. Model derivation and stability characteristics. *Proc. R. Soc. Lond.* A **455**, 2281–2304.

PRICE, J. F. & BARINGER, M. O. 1994 Outflows and deep water production by marginal seas. *Progr. Oceanogr.* **33**, 161–200.

RESZKA, M. K., SWATERS, G. E. & SUTHERLAND, B. R. 2002 Instability of abyssal currents in a continuously stratified ocean with bottom topography. *J. Phys. Oceanogr.* **32**, 3528–3550.

RHINES, P. 1970 Edge-, bottom-, and Rossby waves in a rotating stratified fluid. *Geophys. Fluid Dyn.* **1**, 273–302.

SMITH, P. C. 1975 A streamtube model for bottom boundary currents in the ocean. *Deep-Sea Res.* **22**, 853–873.

SPALL, M. A. & PRICE, J. F. 1998 Mesoscale variability in Denmark Strait: the PV outflow hypothesis. *J. Phys. Oceanogr.* **28**, 1598–1623.

SWATERS, G. E. 1991 On the baroclinic instability of cold-core coupled density fronts on a sloping continental shelf. *J. Fluid Mech.* **224**, 361–382.

SWATERS, G. E. 1998 Numerical simulations of the baroclinic dynamics of density-driven coupled fronts and eddies on a sloping bottom. *J. Geophys. Res.* **103**, 2945–2961.

SWATERS, G. E. & FLIERL, G. R. 1991 Dynamics of ventilated coherent cold eddies on a sloping bottom. *J. Fluid Mech.* **223**, 565–587.

WHITEHEAD, J. A., STERN, M. E., FLIERL, G. R. & KLINGER, B. A. 1990 Experimental observations of baroclinic eddies on a sloping bottom. *J. Geophys. Res.* **95**, 9585–9610.

WHITHAM, G. B. 1974 *Linear and Nonlinear Waves*. Wiley.

WORTHINGTON, L. V. 1969 An attempt to measure the volume transport of Norwegian Sea overflow water through the Denmark Strait. *Deep-Sea Res.* **16**, 421–432.